

Minerva Access is the Institutional Repository of The University of Melbourne

Author/s:

Gransbury, GK;Boulon, ME;Petrie, S;Gable, RW;Mulder, RJ;Sorace, L;Stranger, R;Boskovic, C

Title:

DFT Prediction and Experimental Investigation of Valence Tautomerism in Cobalt-Dioxolene Complexes

Date:

2019-04-01

Citation:

Gransbury, G. K., Boulon, M. E., Petrie, S., Gable, R. W., Mulder, R. J., Sorace, L., Stranger, R. & Boskovic, C. (2019). DFT Prediction and Experimental Investigation of Valence Tautomerism in Cobalt-Dioxolene Complexes. *Inorganic Chemistry*, 58 (7), pp.4230-4243. <https://doi.org/10.1021/acs.inorgchem.8b03291>.

Persistent Link:

<https://hdl.handle.net/11343/333729>

DFT prediction and experimental investigation of valence tautomerism in cobalt-dioxolene complexes

Gemma K. Gransbury[†], Marie-Emmanuelle Boulon[‡], Simon Petrie[§], Robert W. Gable[†], Roger J. Mulder[⊥], Lorenzo Sorace[‡], Robert Stranger[§], Colette Boskovic^{*†}

[†] School of Chemistry, University of Melbourne, VIC 3010, Australia

[‡] UdR INSTM and Department of Chemistry “U. Schiff”, University of Florence, 50019 Sesto Fiorentino (FI), Italy

[§] Research School of Chemistry, College of Physical & Mathematical Sciences, Australian National University, ACT 2601, Australia

[⊥] CSIRO Manufacturing, Clayton, VIC 3168, Australia

Dedicated to Professor Andrea Dei on the occasion of his 75th birthday.

ABSTRACT

The family of complexes of general formula $[\text{Co}(\text{Me}_n\text{tpa})(\text{Xdiox})]^+$ (tpa = tris(2-pyridylmethyl)amine, $n = 0-3$ corresponds to successive methylation of the 6-position of the pyridine rings and $\text{X} = \text{Br}_4, \text{Cl}_4, \text{H}_4, 3,5\text{-Me}_2, 3,5\text{-tBu}_2$) has been investigated by density functional theory (DFT) calculations to predict the likelihood of valence tautomerism (VT). The OPBE

functional with relativistic and solvent corrections has allowed accurate reproduction of trends in spin-state energetics, affording the prediction of VT in complex $[\text{Co}(\text{Me}_3\text{tpa})(\text{Br}_4\text{diox})]^+$ ($\mathbf{1}^+$). One-electron oxidation of neutral precursor $[\text{Co}^{\text{II}}(\text{Me}_3\text{tpa})(\text{Br}_4\text{cat})]$ ($\mathbf{1}$) enabled isolation of target compounds $\mathbf{1}(\text{PF}_6)$ and $\mathbf{1}(\text{BPh}_4)$. Solution variable-temperature UV-Vis absorption and Evans method magnetic susceptibility data confirm DFT predictions that $\mathbf{1}^+$ exists in a temperature-dependent valence tautomeric equilibrium between low spin Co(III)-catecholate and high spin Co(II)-semiquinonate forms. The solution VT transition temperature of $\mathbf{1}^+$ is solvent-tunable with critical temperatures in the range 291-359 K for the solvents measured. Solid-state magnetic susceptibility measurements of $\mathbf{1}(\text{PF}_6)$ and $\mathbf{1}(\text{BPh}_4)$ reveal the onset of VT transitions above room temperature.

INTRODUCTION

Valence tautomerism involves a stimulated and reversible intramolecular electron transfer between a redox-active metal center and a redox-active ligand. Valence tautomeric (VT) transitions may be induced by variation of external stimuli such as temperature, pressure, electric fields, intense magnetic fields (>100 T), light or soft X-rays.¹⁻⁶ Cobalt-dioxolene complexes are excellent candidates for valence tautomerism, as both Co and 1,2-dioxolene (diox) ligands are redox-active, and the VT transition is accompanied by a spin transition at the cobalt center.¹ At low temperature, the low spin (LS) Co(III)-catecholate (cat^{2-}) configuration dominates, while the high spin (HS) Co(II)-semiquinonate (sq^-) state is favored at high temperatures. The electromers can be distinguished by their differing optical spectra, magnetic properties and Co-donor atom bond lengths, which are 0.18-0.21 Å longer in the HS-Co(II)-sq form.⁷ The different physical and

magnetic properties of switchable molecular materials such as VT complexes afford potential applications as sensors and display devices or molecular electronics and spintronics.⁸⁻¹⁰

The bond lengths of the cobalt coordination sphere are longer, and the spin state degeneracy is greater in the HS-Co(II)-sq state compared to the LS-Co(II)-cat one, resulting in a greater entropy (S) for the HS-Co(II)-sq state, which is then stabilized at higher temperatures. It is possible to stabilize the LS-Co(III)-cat state below a critical temperature T_c when the enthalpy change (ΔH) associated with this VT conversion is small and positive with: $T_c = \Delta H/\Delta S$.¹¹ To obtain a ΔH value suitable for the VT transition to occur in accessible temperature range, one strategy is to tune the cobalt(III/II) redox potential to be close to that of the dioxolene semiquinonate/catecholate process. However, in the solid state, the VT process is also governed by crystal packing, counterion and solvate interactions which can influence steepness and hysteresis of the transition as well as its critical temperature.^{1, 12}

Redox tuning via modification of the ancillary ligands to achieve valence tautomerism was exploited by Beni *et al.* with the series $[\text{Co}(\text{Me}_n\text{tpa})(t\text{Bu}_2\text{diox})](\text{PF}_6)$, $n = 0-3$ (tpa = tris(2-pyridylmethyl)amine; Me_ntpa involves successive methylation of the 6-position of the tpa pyridine rings; $t\text{Bu}_2\text{diox} = 3,5\text{-di-tert-butyl dioxolene}$).⁷ Increasing the number of methyl substituents on tpa (n) increases the steric crowding around the Co center (Figure 1), stabilizing the longer bonds of the HS-Co(II) state and increasing the redox potential of Co(III)/Co(II) couple, with very little effect on the dioxolene redox one. In the $[\text{Co}(\text{Me}_n\text{tpa})(t\text{Bu}_2\text{diox})](\text{PF}_6)$ series, the $n = 0$ and 1 analogues exist in the LS-Co(III)-cat state for 0-300 K, $n = 2$ exhibits VT in the solid state and $n = 3$ exists in the HS-Co(II)-sq state in the temperature range 0-300 K.^{7, 13} The redox potential of the dioxolene ligand can also be tuned by varying the substituents on the ring. Dei *et al.* matched the more positive sq/cat redox potential of tetrachlorodioxolene (Cl_4diox) with the higher

Co(III)/Co(II) potential of $\{\text{Co}(\text{Me}_3\text{tpa})\}$ to access a VT transition for $[\text{Co}(\text{Me}_3\text{tpa})(\text{Cl}_4\text{diox})]^+$ in solution.¹¹

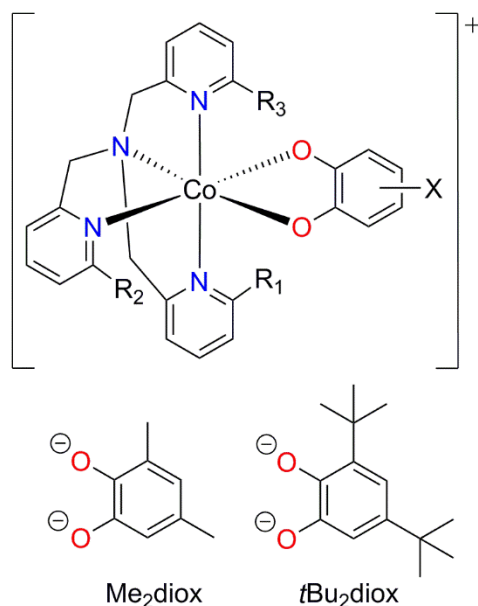


Figure 1. Family of complexes $[\text{Co}(\text{Me}_n\text{tpa})(\text{Xdiox})]^+$; R_1, R_2 and $R_3 = \text{H}$ or Me ; $X = \text{Br}_4, \text{Cl}_4, \text{H}_4, 3,5\text{-Me}_2, 3,5\text{-}t\text{Bu}_2$.

In principle, density functional theory (DFT) can use relative spin-state energies to predict whether compounds are likely to exhibit valence tautomerism prior to their synthesis. In practice there exists a wide range of available DFT functionals without a universally accurate functional for spin-state energies.¹⁴⁻¹⁵ Generalized Gradient Approximation (GGA) functionals such as BP86 give reliable molecular geometries but underestimate the stability of the high spin states while the incorporation of Hartree-Fock (HF) exchange may over-stabilize the high spin states, such as in the widely-used B3LYP hybrid functional (20% HF exchange).¹⁶⁻¹⁹ In the field of molecular switchable materials Reiher *et al.* developed a reparametrized hybrid functional B3LYP* with

15% HF exchange to give accurate spin-state energies for a series of Fe(II) spin crossover (SCO) complexes; however, the ideal amount of HF exchange has been found to depend on metal, oxidation state and property of interest.¹⁹⁻²¹ This is of particular concern for VT prediction where the oxidation state of the metal changes, in contrast to SCO.

Different DFT functionals will result in different spin state energetics but these functional-dependent biases are consistent within families of related complexes. Given accurate energetics for one transition metal complex, the DFT method can accurately predict spin state energies for similar compounds.²² The GGA functional OPBE; hybrid functional B3LYP* and the meta-hybrid functional TPSSh have all been found to give accurate spin state energetics for some Co VT or transition metal spin crossover (SCO) systems.²³⁻²⁹ In particular, OPBE is cost-efficient and has given accurate spin-state energetics in many Fe(II) and Fe(III) SCO systems,³⁰⁻³⁵ and some Co SCO and VT systems^{26, 36-37} In Sato's 2010 study on the VT mechanism in [Co(bpy)(H₄diox)₂] (bpy = 2,2'-bipyridine), both B3LYP* and OPBE accurately reproduced the energy separation between the relevant doublet and sextet states; however, OPBE was unable to reproduce the ordering of the quartet state, which experimentally lies above the sextet state. Minkin, Starikova and Starikov have been prolific in using the B3LYP* functional and 6-311++G(d,p) basis set to model some experimental Co VT compounds,³⁸ and predict VT in a wide range of complexes yet to be verified by experiment, in particular focusing on neutral adducts of Co diketonates, aminovinylketonates and diimines with redox-active ligands.³⁹⁻⁴³ We have also included the related hybrid functional PBE0 and meta-GGA functional TPSS for comparison.⁴⁴⁻⁴⁷

Some members of the [Co(Me_ntpa)(Xdiox)]⁺ series have been investigated with DFT previously to simulate infrared (IR) spectra ($n = 0, 3$; X = 3,5-*t*Bu₂),⁴⁸ investigate the possibility of electric field induced VT ($n = 2$),⁵ and examine spin state energetics ($n = 2$; X = 3,5-*t*Bu₂).⁴⁹

Infrared spectra were successfully generated using the B3LYP functional but this functional gave an incorrect spin ground state after geometry optimization of the complex.^{5, 48} Most recently, Starikova *et al.* investigated the charged complexes $[\text{Co}(\text{Me}_n\text{tpa})(\text{H}_4\text{diox})]^+$ ($n = 0, 2, 3$) and $[\text{Co}(\text{AzaNR})(\text{Xdiox})]^+$ (AzaNR = *N,N'*-di-*tert*-butyl- and *N,N'*-dimethyl-2,11-diaza[3.3]-(2,6)pyridinophane; X = H₄, Cl₄) using the TPSSh functional.⁴⁹ The authors observed that inclusion of counterions in the calculations improved prediction of the ground state compared to experiment. However, it must be noted that the experimental complexes for which the DFT results were compared were not the same as the calculated complexes, as they possessed *tert*-butyl substituted dioxolenes, and the substitution of a dioxolene has a significant effect on the redox potential and therefore enthalpy of the VT transition.^{7, 50} While counterions are often not included in DFT calculations, condensed-phase environmental effects are critical in modelling the geometric structure of coordination complexes especially in the case of mixed anionic and neutral ligands such as dioxolenes and the tpa series.⁵¹⁻⁵²

The aim of this work was to apply DFT methodology to identify new members of the family $[\text{Co}(\text{Me}_n\text{tpa})(\text{Xdiox})]^+$ ($n = 0-3$, X = Br₄, Cl₄, H₄, 3,5-Me₂, 3,5-*t*Bu₂) that might exhibit a VT transition. To achieve our aim, we needed to first benchmark DFT functionals, using experimental data reported previously for different members of the structural family. This allowed us to select the most appropriate methodology for spin-state energy calculations, which was then employed to predict a candidate complex for VT. Finally, the identified target complex, $[\text{Co}(\text{Me}_3\text{tpa})(\text{Br}_4\text{diox})]^+$, was synthesized, with subsequent structural, magnetic and electronic characterization in solution and solid state validating the outcome of the calculations.

RESULTS AND DISCUSSION

DFT Results. In this work, we examined the family $[\text{Co}(\text{Me}_n\text{tpa})(\text{Xdiox})]^+$ ($n = 0-3$, $\text{X} = \text{Br}_4, \text{Cl}_4, \text{H}_4, 3,5\text{-Me}_2, 3,5\text{-}t\text{Bu}_2$; Figure 1). Each of these complexes was optimized in the diamagnetic LS-Co(III)-cat state and the paramagnetic HS-Co(II)-sq state to evaluate the potential for VT behavior, as these are the two states observed experimentally with tpa derived ligands.⁷ Valence tautomerism has been shown to occur as a single barrier process between the LS-Co(III)-cat and HS-Co(II)-sq states, so the LS-Co(II)-sq triplet state, which is not observed experimentally, does not need to be considered as an intermediate.²⁶ Modelling the exchange coupling between HS-Co(II) and the semiquinonate radical is non-trivial.⁵³ A *pseudo*-octahedral Co(II) ion has significant spin-orbit coupling and as such the final HS Co(II)-sq ground state is a spin-orbit coupled admixture of the quintet and triplet states, which cannot be treated adequately with DFT and requires a multiconfigurational approach.⁵⁴ In the present work, we have used the quintet state to represent the HS-Co(II)-sq valence tautomer and have not focused on the broken symmetry triplet state. The states were identified, first using the spin density distribution over the complex (Figure S15), and second by the charge distribution.⁵⁵ A series of geometry optimizations was performed to identify the most stable isomers, as detailed in the supporting information (S.I.-8).

Functional optimization. We trialed GGA functionals BP86 and OPBE; meta-GGA functional TPSS; hybrid functionals PBE0 ($c_3 = 0.25$), B3LYP ($c_3 = 0.20$) and B3LYP* ($c_3 = 0.15$); and the meta-hybrid functional TPSSh ($c_3 = 0.10$) for determining the enthalpy of the VT transition (ΔH) evaluated as the difference in spin state energies between the two valence tautomers: $E(\text{HS-Co(II)-sq, quintet}) - E(\text{LS-Co(III)-cat, singlet})$.^{16-18, 20, 23-25, 44-47} All calculations were performed with geometry optimization using the relativistically contracted equivalent of the TZP basis set, ZORA relativistic correction and COSMO solvent model with acetonitrile (MeCN).⁵⁶⁻⁶⁰ Initial

functional screening (Table 1) was performed on the VT complex $[\text{Co}(\text{Me}_2\text{tpa})(t\text{Bu}_2\text{diox})]^+$, for which an approximate ΔH of 6 kJ mol^{-1} has been derived from voltammetric measurements in MeCN assuming that $\Delta S = +50 \text{ J K}^{-1} \text{ mol}^{-1}$.⁷ Values of ΔH from voltammetry were chosen to benchmark the DFT results as they are available for the whole series $[\text{Co}(\text{Me}_n\text{tpa})(t\text{Bu}_2\text{diox})]^+$ ($n = 0-3$).⁷ Experimental values of ΔH for VT transitions are an alternative choice to benchmark ΔH and take values in the range $14.2-38.4 \text{ kJ mol}^{-1}$ for 1:2 Co:diox complexes.⁶¹⁻⁶³ However, ΔH has only been reported previously for $[\text{Co}(\text{Me}_3\text{tpa})(\text{Cl}_4\text{diox})]^+$, as 31.2 kJ mol^{-1} in dichloromethane (DCM) solution.¹¹ We found that the BP86, TPSS and TPSSh functionals over-stabilized the LS-Co(III)-cat state while PBE0 and B3LYP gave an incorrect HS-Co(II)-sq ground state. The OPBE and B3LYP* functionals agree within the 12 kJ/mol (3 kcal/mol) accepted error for DFT spin state energetics. We have chosen to use the OPBE functional as it affords the best agreement with experimental values for the sign and magnitude of ΔH for $[\text{Co}(\text{Me}_2\text{tpa})(t\text{Bu}_2\text{diox})]^+$ (Table 1) and has been used to give accurate spin-state energies for cobalt VT complexes previously.³⁷

Table 1. Functional-dependence of ΔH for $[\text{Co}(\text{Me}_2\text{tpa})(t\text{Bu}_2\text{diox})]^+$

Functional ^a	$\Delta H^b / \text{kJ mol}^{-1}$
BP86	62.5
OPBE	8.2
PBE0	-43.9
B3LYP	-32.3
B3LYP*	-3.4
TPSS	63.4
TPSSh	287.3

^a Calculations performed with relativistically contracted TZP basis set, ZORA relativistic correction and COSMO solvent correction. ^b Experimentally $\Delta H \sim 6 \text{ kJ mol}^{-1}$ ref.7

Application to VT prediction. Following functional optimization, the OPBE/TZP/ZORA/COSMO method was then applied to the entire family $[\text{Co}(\text{Me}_n\text{tpa})(\text{Xdiox})]^+$ (Table 2). As the number of Me substituents on the tpa increases, the HS-Co(II)-sq state is stabilized, consistent with greater steric hindrance favoring longer Co-O/N bonds which are present in the HS-Co(II) state. The HS-Co(II)-sq state is also stabilized by more electron donating dioxolene substituents, as predicted from the redox potentials of the uncoordinated dioxolenes;⁶⁴ the exception being the larger ΔH for Br₄diox complexes over Cl₄diox complexes for $n = 0-2$ despite the greater the reduction potential of tetrachlorocatechol over tetrabromocatechol. A common practice with DFT calculations is to remove *tert*-butyl groups or replace them with methyl groups to simplify the calculations and decrease the computational time. However, for the present compounds, the HS-Co(II)-sq state is significantly stabilized by the electron-donating *tert*-butyl substituents on the dioxolene, by an average of 21 kJ mol⁻¹ compared to an unsubstituted dioxolene, or 11 kJ mol⁻¹ for methyl group replacement. We recommend that electronically important substituents on redox-active ligands should not be eliminated or substituted in DFT calculations, lest there be significant errors in the relative energies obtained.

Table 2. Calculated ΔH for the $[\text{Co}(\text{Me}_n\text{tpa})(\text{Xdiox})]^+$ family ($n = 0-3$) using the OPBE/TZP/ZORA/COSMO method with MeCN

X	$\Delta H / \text{kJ mol}^{-1}$			
	$n = 0$	$n = 1$	$n = 2$	$n = 3$
<i>t</i> Bu ₂ ^a	61	34	6	-25
<i>t</i> Bu ₂	51.9	33.1	8.1^b	-17.1
Me ₂	64.4	44.4	20.3	-9.3
H ₄	73.5	53.8	29.6	3.4^c
Cl ₄	84.9	63.7	38.3	12.3^b
Br ₄	88.5	66.1	45.6	11.7^c

^a Experimental values.⁷ ^b VT transition observed experimentally.^{7, 11, 13} ^c Predicted by DFT calculations as most likely to exhibit VT behavior at practically accessible temperatures.

Based on the experimental observation of VT for complexes $[\text{Co}(\text{Me}_2\text{tpa})(\textit{t}\text{Bu}_2\text{diox})]^+$ and $[\text{Co}(\text{Me}_3\text{tpa})(\text{Cl}_4\text{diox})]^+$,^{7, 11, 13} we predict that complexes with LS-Co(III)-cat ground states and values of ΔH in the range 8-12 kJ mol⁻¹ have potential to exhibit a VT transition in the practically accessible temperature range up to around 400 K. Complex $[\text{Co}(\text{Me}_3\text{tpa})(\text{Cl}_4\text{diox})]^+$ displays a VT transition in a DCM solution around 250 K and was calculated to have a ΔH at the upper end of the VT range (12.3 kJ mol⁻¹ in MeCN). Using DCM in the COSMO solvent model gives a ΔH value of 8.2 kJ mol⁻¹, which agrees within error with the value in acetonitrile.

From the data in Table 2, we predict previously unreported complexes $[\text{Co}(\text{Me}_3\text{tpa})(\text{Br}_4\text{diox})]^+$ and $[\text{Co}(\text{Me}_3\text{tpa})(\text{H}_4\text{diox})]^+$ as candidates for valence tautomerism. As ΔH is below the range for established VT complexes, we expect $[\text{Co}(\text{Me}_3\text{tpa})(\text{H}_4\text{diox})]^+$ to either have a HS-Co(II)-sq ground state or display VT at a low transition temperature. The predicted ΔH values for $[\text{Co}(\text{Me}_n\text{tpa})(\text{H}_4\text{diox})]^+$ ($n = 0, 2, 3$) are larger than the values obtained by Starikova *et al.* using

the TPSSh functional with counterion: 50.6, 12.6 and 1.3 kJ mol⁻¹ (24.6, -13.0, -30.5 kJ mol⁻¹ without counterion). From the DFT results we predict that [Co(Me₃tpa)(Br₄diox)]⁺ (**1**⁺) should exhibit a VT transition close to room temperature in MeCN, with a ΔH of 11.7 kJ mol⁻¹ at the upper end of the VT range. Complex [Co(Me₃tpa)(Br₄diox)]⁺ (**1**⁺) was thus identified as the primary synthetic target for this work.

Syntheses. The cobalt(II) precursor to the target VT complex, previously unreported [Co(Me₃tpa)(Br₄cat)] (**1**), was prepared by combining equimolar amounts of cobalt(II) perchlorate with appropriate safety precautions, tri(6-methyl-2-pyridylmethyl)amine and tetrabromocatecholate. Neutral complex **1** precipitates directly from the reaction solution as a red solid in high yield (94%) and was recrystallized from DMF/diethyl ether. The zinc analogue [Zn(Me₃tpa)(Br₄cat)] (**1-Zn**), was synthesized to provide a comparison for spectral and electrochemical properties and was synthesized as per **1** using zinc(II) chloride in place of the cobalt salt. The infrared spectra (Figure S2) and powder X-ray diffraction patterns (Figure S8) of **1** and **1-Zn** confirm the compounds are isostructural and isomorphous, respectively.

Two salts of **1**⁺ were synthesized by 1e-oxidation of **1** (see electrochemistry section) using ferrocenium salts. The synthesis is complicated by (i) the low solubility of **1** in all solvents except DMF, (ii) air sensitivity of the ferrocenium salt in solution, (iii) water sensitivity of the oxidation, (iv) similar solubility of the product and ferrocenium salt and (v) the formation of side products and slow reduction of **1**⁺ back to **1** in methanol solution over one week.

Compound [Co(Me₃tpa)(Br₄diox)](PF₆) (**1(PF₆)**) was synthesized by oxidizing a DMF suspension of **1** with ferrocenium hexafluorophosphate. The bulk solid recrystallized from toluene analyzed crystallographically as **1(PF₆)**·2tol, although partial desolvation upon air drying affords **1(PF₆)**·1.2tol by elemental and thermogravimetric analysis (Figure S1). The powder X-ray

diffraction pattern for **1**(PF₆)·1.2tol (Figure S9) matches well with the pattern calculated from the single crystal structure of **1**(PF₆)·2tol. While more volatile solvents such as acetone or methanol would be more desirable for isolation and did result in small quantities of **1**(PF₆), the very low solubility of **1** and lack of reproducibility of the reaction in acetone, methanol and MeCN prohibited a bulk synthesis of **1**(PF₆) in these solvents.

Compound [Co(Me₃tpa)(Br₄diox)](BPh₄) (**1**(BPh₄)) was synthesized from **1** and ferrocenium tetraphenylborate in a heterogeneous sonication reaction, as developed by Tezgerevska *et al.*, in which only the by-product ferrocene is soluble in the isopropanol solvent.⁶⁵ This reaction is almost quantitative (97%), allows simple isolation of the product by filtration and avoids difficulties created by oxidizing **1** in solution. Compound **1**(BPh₄) was recrystallized solvent-free from DCM/diethyl ether and the purity of the bulk sample was confirmed by elemental and thermogravimetric analysis (Figure S1) and powder X-ray diffraction (Figure S10). The infrared spectra (Figure S3) of **1**(PF₆)·1.2tol and **1**(BPh₄) are consistent with the presence of a common complex cation. Attempts to synthesize the other VT candidate complex [Co(Me₃tpa)(H₄diox)]⁺ were unsuccessful.

Structure Description. The crystal data for compounds **1**, **1**-Zn, **1**(PF₆)·2tol and **1**(BPh₄) are presented in Tables S1 and S2. Compounds **1** and **1**-Zn are isomorphous and crystallize in the monoclinic space group *P2₁/n* with one unique metal complex in the asymmetric unit. Compound **1**(BPh₄) crystallizes in the monoclinic space group *P2₁/c* with two crystallographically unique cobalt complexes in the asymmetric unit, two BPh₄⁻ anions and no solvent. Compound **1**(PF₆)·2tol crystallizes in the tetragonal space group *P4₂/n* and displays one crystallographically unique cobalt complex in the asymmetric unit, one PF₆⁻ anion and two toluene molecules, one of which is disordered. On increasing temperature from 100 to 380 K, the cell parameters of **1**(PF₆)·2tol

increase by 0.6-2.0% and the total cell volume increases by 4.8% (Table S2). This expansion is consistent with increased thermal parameters at higher temperatures rather than a VT transition.

The metal complexes in compounds **1**, **1-Zn**, **1(PF₆)·2tol** and **1(BPh₄)** share a common structural motif (Figure 2). Selected experimental structural data for the four compounds are available in Table 3, together with DFT calculated parameters for the sake of comparison. The complexes consist of 6-coordinate metal center with a N₄O₂ donor set comprised of three pyridyl N and one tertiary amine N from the tripodal tetradentate Me₃tpa ligand, and two *cis* O atoms from tetrabromodioxolene. Examination of the Co coordination sphere for **1** indicates a distorted octahedral environment with an octahedral *SHAPE* index of 1.730 and Co-O, Co-N_{amine} and Co-N_{py} bond distances in the ranges 1.985(1)-2.061(1), 2.129(2) and 2.229(2)-2.267(2) Å.⁶⁶⁻⁶⁷ The bond lengths are consistent with HS-Co(II) and the DFT-optimized HS-Co(II)-cat structure (Table 3).⁶⁸ The empirical metrical oxidation state (MOS) of dioxolene ligands, proposed by Brown *et al.*, uses a least squares fitting of C-C and C-O bond lengths to assign an apparent oxidation state: -1 for a semiquinonate ligand and -2 for a catecholate ligand.⁶⁹ The MOS values for Br₄cat²⁻ in **1** and **1-Zn** are both -1.5(2); the MOS is considered unreliable for electron-poor dioxolenes so comparison to the value of -1.4(2) in the DFT-optimized HS-Co(II)-cat structure confirms the tetrabromodioxolene is present in the catecholate form.⁶⁹ All structural data are thus consistent with HS-Co(II)-cat formulation for **1** and Zn(II)-cat for **1-Zn**.

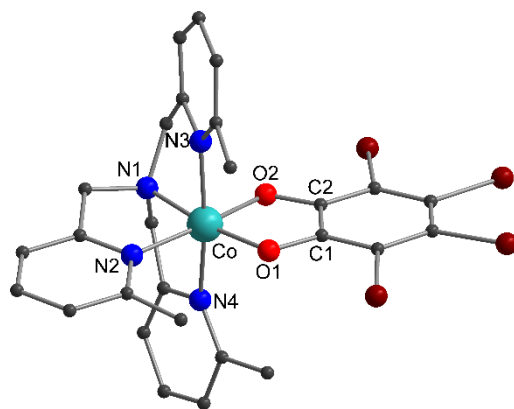


Figure 2. Structure of 1^+ in $1(\text{PF}_6)\cdot 2\text{tol}$. Color code: carbon, black; oxygen, red; nitrogen, blue; cobalt, aqua green; bromine, brown.

Table 3. Selected Interatomic Distances (Å), Distortion Parameters and Oxidation State Parameter for Compounds **1**, **1-Zn**, **1(PF₆)-2tol**, **1(BPh₄)** and DFT optimized **1** and **1⁺** with OPBE/TZP/ZORA/COSMO

	1	1 (DFT)	1-Zn	1(PF₆)-2tol		1(BPh₄)		1⁺ (DFT)	
	130 K	HS-Co(II)-cat	130 K	100 K	380 K	100 K	100 K	LS-Co(III)-cat	HS-Co(II)-sq
						molecule A	molecule B		
Interatomic Distances									
M-O1	1.985(1)	1.966	1.975(2)	1.889(2)	1.886(4)	1.878(2)	1.872(3)	1.881	1.946
M-O2	2.061(1)	2.040	2.062(3)	1.887(2)	1.892(5)	1.886(2)	1.884(2)	1.875	2.025
M-N1	2.129(2)	2.118	2.139(3)	1.944(3)	1.938(5)	1.930(3)	1.939(3)	1.927	2.101
M-N2	2.229(2)	2.205	2.239(3)	2.029(3)	2.036(7)	2.011(3)	2.003(3)	2.028	2.166
M-N3	2.267(2)	2.222	2.292(3)	2.004(3)	2.006(6)	1.991(3)	1.987(3)	2.006	2.311
M-N4	2.253(2)	2.343	2.355(3)	2.018(3)	2.015(6)	1.991(3)	1.996(3)	2.043	2.204
O1-C1	1.313(2)	1.305	1.315(4)	1.327(4)	1.303(8)	1.312(4)	1.317(4)	1.324	1.296
O2-C2	1.296(2)	1.294	1.296(4)	1.330(4)	1.335(8)	1.325(4)	1.328(4)	1.323	1.287
C1-C2	1.451(3)	1.447	1.456(4)	1.401(4)	1.373(9)	1.411(4)	1.397(5)	1.411	1.445
Distortion Parameters and Oxidation State Parameter									
SHAPE (Oh) ^a	1.730	1.471	1.918	0.486	0.558	0.504	0.420	0.634	1.493
Σ ^o ^b	101.0	82.3	104.0	51.4	55.3	50.4	47.3	54.3	86.4
Θ ^o ^c	172.6	164.4	170.8	69.4	104.3	78.2	69.7	87.9	147.6
MOS ^d	-1.5(2)	-1.4(2)	-1.5(2)	-1.8(1)	-1.9(2)	-1.9(2)	-1.8(2)	-1.7(1)	-1.5(1)

^a SHAPE index for octahedral geometry, calculated in *SHAPE 2.1*.⁶⁶⁻⁶⁷

^b $\Sigma = \sum_{i=1}^{12} |90 - \alpha_i|$ where α_i are the twelve *cis*-O/N-Co-O/N angles about the cobalt atom.⁷⁰

^c $\Theta = \sum_{j=1}^{24} |60 - \theta_j|$ where θ_j are the 24 unique O/N-C_a-C_b-O/N dihedral angles, $|\theta_j| < 120^\circ$. C_a and C_b are the centroids of two triangular faces that are opposite on the octahedron such that C_a-C_b represents their common *pseudo*-threefold axis.⁷⁰

^d Metrical Oxidation State, as described in main text.⁶⁹

Complex $\mathbf{1}^+$ is common to $\mathbf{1}(\text{PF}_6)\cdot 2\text{tol}$ and $\mathbf{1}(\text{BPh}_4)$; at 100 K, the Co coordination geometry in $\mathbf{1}^+$ is octahedral with minimal distortion as evidenced by octahedral *SHAPE* indices in the range 0.420-0.504 and small Σ and Θ distortion parameters (Table 3, footnotes).^{66-67, 70} The coordination sphere displays Co-O, Co-N_{amine} and Co-N_{py} bond distances in the ranges 1.872(3)-1.892(5), 1.930(3)-1.944(3) and 1.987(3)-2.029(3) Å respectively. The bond distances and minimal distortion from octahedral symmetry are characteristic of a LS-Co(III) center and show close agreement with the DFT optimized structure in the LS-Co(III)-cat state. The MOS values of the tetrabromodioxolene ligand in $\mathbf{1}(\text{PF}_6)\cdot 2\text{tol}$ and $\mathbf{1}(\text{BPh}_4)$ at 100 K are -1.8(2) and -1.9(2), respectively; comparison to the MOS of the LS-Co(III)-cat and HS-Co(II)-sq DFT optimized structures of $\mathbf{1}^+$ indicate the tetrabromodioxolene exists in the catechol state at 100 K for both compounds. All structural data are thus consistent with $\mathbf{1}^+$ in both $\mathbf{1}(\text{PF}_6)\cdot 2\text{tol}$ and $\mathbf{1}(\text{BPh}_4)$ in the LS-Co(III)-cat state at 100 K.

Upon increase in temperature, there is no significant change in Co-O/N bond lengths of $\mathbf{1}(\text{PF}_6)\cdot 2\text{tol}$ up to 380 K (Figure S4). The high temperature structure of $\mathbf{1}(\text{PF}_6)\cdot 2\text{tol}$ shows slightly larger octahedral *SHAPE*, Σ and Θ distortion parameters with similar Co-O/N bond lengths and MOS of -1.9(2) indicating $\mathbf{1}(\text{PF}_6)\cdot 2\text{tol}$ still exists in the LS-Co(III)-cat state at 380 K. The variable temperature crystallographic data are consistent with no VT transition for $\mathbf{1}(\text{PF}_6)\cdot 2\text{tol}$ up to 380 K.

Crystal packing diagrams for compounds $\mathbf{1}$, $\mathbf{1-Zn}$, $\mathbf{1}(\text{PF}_6)\cdot 2\text{tol}$ and $\mathbf{1}(\text{BPh}_4)$ are available in Figures S5-S7. While one of the toluene molecules in compound $\mathbf{1}(\text{PF}_6)\cdot 2\text{tol}$ lies in a cavity surrounded by the cations and anions, it is evident that the disordered molecules of toluene solvent are located in open channels which lie along the *c*-axis, with the molecules being situated around a 4_2 screw and C_2 rotation axis. Partial desolvation to $\mathbf{1}(\text{PF}_6)\cdot 1.2\text{tol}$ was evident upon air drying, most likely involving the loss of the toluene molecules situated in the

channels, although the crystal structural analyses indicated no evidence of solvent loss up to 380 K for single crystals of **1(PF₆)·2tol** that were immersed in cryoprotectant oil.

Solid-State Magnetic Measurements. Variable-temperature magnetic susceptibility measurements (χ_M is molar magnetic susceptibility) were performed on solid samples of **1(PF₆)·1.2tol** and **1(BPh₄)** (Figure 3). Compound **1(PF₆)·1.2tol** exhibits a $\chi_M T$ value of 0.13 cm³ K mol⁻¹ at 1.8 K which gradually increases to 0.34 cm³ K mol⁻¹ at 270 K, followed by a more rapid increase to 0.66 cm³ K mol⁻¹ at 360 K. The first cooling cycle shows a more gradual decrease over the entire temperature range recovering a $\chi_M T$ value of 0.14 cm³ K mol⁻¹ at 1.8 K and a repeated heating and cooling cycle is superimposable on the first cooling curve.

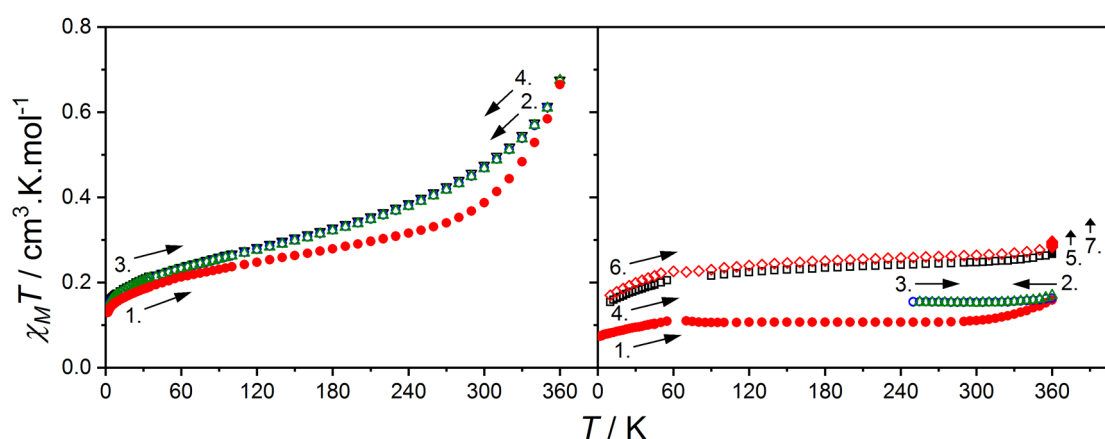


Figure 3. LEFT. Plot of $\chi_M T$ versus T for solid state **1(PF₆)·1.2tol** on first heating 1.8–360 K (solid red circles), first cooling 360–2 K (open blue circles), second heating 2–360 K (open green triangles) and second cooling 360–1.8 K (open black triangles). RIGHT. Plot of $\chi_M T$ versus T for solid state **1(BPh₄)** on first heating 1.9–360 K (solid red circles), first cooling 360–250 K (open blue circles), second heating 250–360 K (open green triangles), third heating 10–360 K (open black squares), first holding at 360 K for several hours (solid black squares), fourth heating 10–360 K (open red diamonds) and second holding at 360 K for several hours (solid red diamonds). Numbered arrows indicate the order of the measurements.

The LS-Co(III)-cat species is diamagnetic therefore the non-zero χ_{MT} value of **1(PF₆)·1.2tol** at 1.8 K arises from the temperature-independent paramagnetism (TIP) of Co(III) and a small trapped fraction of HS-Co(II)-sq at low temperatures, which is common for cobalt-dioxolene systems.^{13, 68, 71} The rapid increase of χ_{MT} between 270 and 360 K corresponds to a 21% VT transition, based on a maximum attainable χ_{MT} value of 3.17 cm³ K mol⁻¹ (Evans method data in 1,2-dichloroethane, DCE). The highest temperature accessible in the SQUID magnetometer was 360 K, and the χ_{MT} value is expected to increase above this temperature.

The relatively low percentage VT conversion for **1(PF₆)·1.2tol** up to 360 K is consistent with variable temperature crystallographic data for **1(PF₆)·2tol**, which indicate a majority of LS-Co(III)-cat centers at 380 K. The more gradual VT transition on repeated heating-cooling cycles is usually associated with a permanent structural rearrangement often following solvent loss.^{68, 72-73} Thermogravimetric analysis (Figure S1) indicates minimal (< 0.1%) mass loss at 360 K compared to 380 K (6.5%) suggesting that this is not the case here. However, the pressed PTFE pellet may behave differently to the microcrystalline powder.

Compound **1(BPh₄)** exhibits a χ_{MT} value of 0.07-0.11 cm³ K mol⁻¹ in the range 1.9-300 K (Figure 3, right). On heating, a gradual, irreversible increase in χ_{MT} is observed, reaching to 0.16 cm³ K mol⁻¹ at 360 K. Further heating cycles (10–360 K) confirm the transition to be slow and irreversible, reaching a maximum χ_{MT} of 0.30 cm³ K mol⁻¹. Below 300 K the trapped HS-Co(II)-sq fraction can be estimated as 2–3%, with compound **1(BPh₄)** undergoing a gradual, incomplete, irreversible and slow VT transition on heating. At the completion of the first heating cycle the percent conversion is estimated as 5%, which increases to 9% after multiple heating-cooling cycles and holding at 360 K. Irreversible and kinetically slow transitions have been observed in Co-dioxolene systems previously.^{11, 74}

UV-Visible Spectroscopy. There are few reports of UV-Vis spectra on Co(II)-cat species due to their low solubility. Spectra of Co(II)-cat species formed *in situ* have revealed

weak bands at 469, 562 and 615 nm(sh) ($\epsilon = 34\text{-}52 \text{ M}^{-1} \text{ cm}^{-1}$), or very broad almost featureless spectra with absorptions centered on 450-550 nm and $\sim 600 \text{ nm}$ ($\epsilon \sim 1.5 \times 10^3 \text{ M}^{-1} \text{ cm}^{-1}$).^{68, 75} In contrast, the spectrum for the red solution of **1** in DMF is dominated by an intense, sharp absorption centered at 440 nm, which is not present for the yellow solution of **1-Zn** (Figure 4). The band is thus not ligand based and is too intense for a d-d transition, so is tentatively assigned as a charge transfer transition of unknown origin. Complex **1** also displays shoulders at 497, 543 and 567 nm assigned as the ${}^4\text{T}_1({}^4\text{P}) \leftarrow {}^4\text{T}_1({}^4\text{F})$ d-d transitions of *pseudo*-octahedral HS-Co(II) ion.⁷⁶⁻⁷⁷ Additional ${}^4\text{T}_2({}^4\text{F}) \leftarrow {}^4\text{T}_1({}^4\text{F})$ transitions are expected to lie just above the wavelength range of the spectrometer. The spectra for **1** and **1-Zn** display a shoulder at 377 and 408 nm, respectively, which are likely due to analogous ligand-centered transitions.

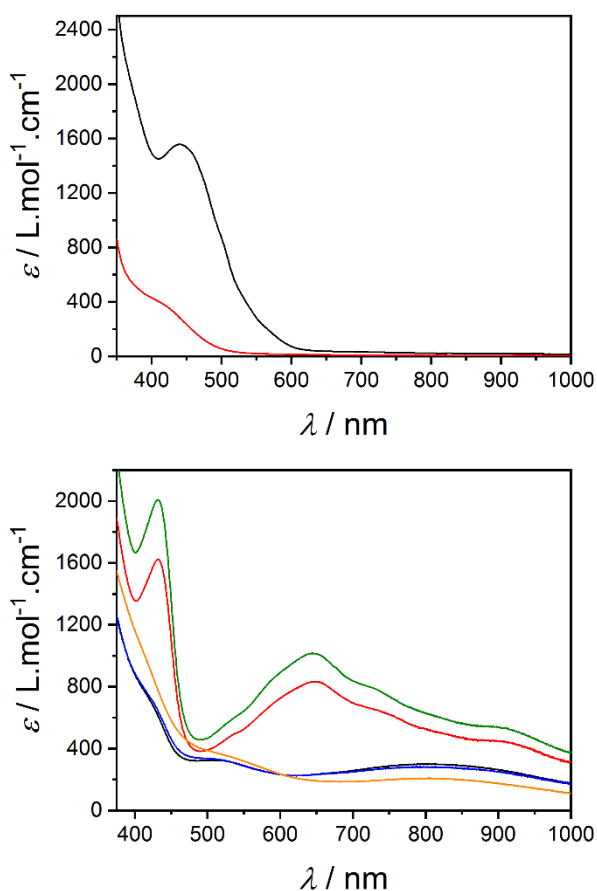


Figure 4. Room temperature UV-Visible spectra of (top) **1** (black) and **1-Zn** (red) in DMF and (bottom) **1⁺** in MeCN (black), acetone (blue), DMF (orange), DCE (red) and DCM (green).

The UV-Vis spectrum of **1**(PF₆) in MeCN at room temperature (Figure 4) is characteristic of the LS-Co(III)-cat tautomer.^{7,68} Comparison to the spectra of LS-Co(III)-cat [Co(Me₃tpa)(Cl₄cat)](PF₆) in MeCN allows assignment of the bands at 414 and 803 nm as ligand-to-metal charge transfers and the band at 508 nm as a ¹T₁ ← ¹A₁ transition in octahedral symmetry.¹¹ While the spectra of **1**⁺ in acetone and DMF at room temperature are also characteristic of the LS-Co(III)-cat electronic state, a solution of **1**⁺ in DCM or 1,2-dichloroethane (DCE) is bright green rather than brown and the spectral characteristics suggest the HS-Co(II)-sq state dominates. Comparison of the DCM spectrum to that of [Co(Me₃tpa)(Cl₄sq)](PF₆) and [Co(Me₃tpa)(*t*Bu₂sq)](PF₆) allows assignment of the band at 647 nm and shoulders in the range 500-650 nm as metal-to-ligand charge transfers (MLCTs) and shoulders at 700-1000 nm as internal ligand transitions.¹¹ The major band at 432 nm may be a ligand-based transition or a charge transfer band, as observed for **1**.

Variable temperature UV-Vis spectra of **1**(PF₆) in MeCN (Figure 5) and DCE (Figure S11) were recorded in the range 283 to 348 K and 283 to 343 K respectively. The UV-Vis spectra show the emergence of HS-Co(II)-sq bands on heating, clearly observed at 423 nm and 648 nm. Similar bands are observed at 432 and 647 nm in the room temperature DCM spectrum (Figure 4) and at 435 and 641 nm in the DCE spectra (Figure 4 and S11). The room temperature spectra were recovered on cooling, and the color change of the MeCN solution of **1**(PF₆) from dark brown at 283 K to bright green at 348 K was reproduced on multiple heating and cooling cycles, consistent with a reversible thermally-induced VT transition. The rate of increase of the MLCT band around 650 nm suggests that *T_c* is above 348 K in MeCN and around 293 K in DCE. No isosbestic points were observed; however, this is consistent with the higher absorbance of the HS-Co(II)-sq state than LS-Co(III)-cat over the entire range 375-1000 nm. The qualitative agreement in the HS-Co(II)-sq bands between the 348 K MeCN spectrum and the DCM and DCE spectra are consistent with the presence of only two species in solution.

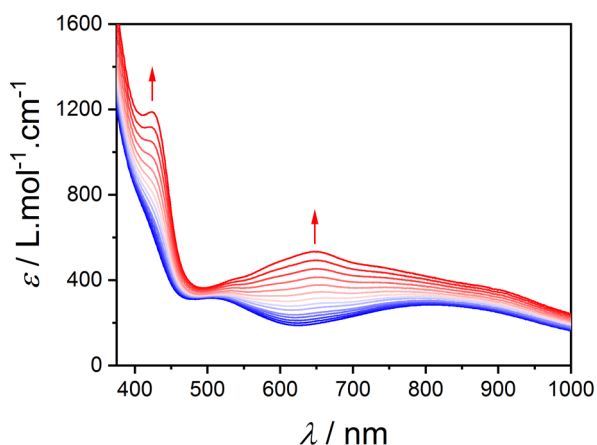


Figure 5. Temperature-dependence of the UV-visible spectrum of 1^+ in MeCN from 283 K (blue) to 348 K (red) in 5 K intervals.

The choice of solvent modulates the relative stability of the two valence tautomers and tunes the VT interconversion temperature. In addition to the spectra above, a green color was observed during the recrystallization of crude $1(\text{PF}_6)$ from toluene when heating above 343 K; however, UV-Vis analysis was precluded due to the low solubility after recrystallization. Combining this observation with the UV-Vis spectra above gives the following trend for T_C : $\text{DCM} < \text{DCE} < \text{acetone} \approx \text{MeCN} < \text{toluene}$. Enthalpy changes for VT transitions have been found to correlate with the donor strength of the solvent; however, this does not appear to be the case here suggesting either the presence of specific solvent-complex interactions or competing stabilizing effects.^{11, 78-79} The ability of chlorinated solvents to stabilize the HS-Co(II)-sq state and shift the VT interconversion to lower temperatures has been reported previously.¹¹

Solution Magnetic Susceptibility. Magnetic susceptibility measurements of $1(\text{PF}_6)$ in deuterated MeCN, DCM or DCE were performed using the Evans NMR method.⁸⁰⁻⁸¹ The temperature range of the experiments were chosen to be above the freezing temperatures so

that the three samples were in the liquid state. Measurements were not performed on **1(BPh₄)** due to its limited solubility. Gradual increases in $\chi_M T$ were observed in all three solvents (Figure 6), ranging from 0.3-1.2 cm³ K mol⁻¹ in MeCN, 0.4-2.0 cm³ K mol⁻¹ in DCM and 0.7-2.7 cm³ K mol⁻¹ in DCE, confirming the presence of a solvent-tunable thermal VT transition. In DCE the VT transition was centered in the accessible temperature window allowing levelling of the data to be observed at both temperature extremes. To obtain the thermal parameters in Table 4, the susceptibility data for each solvent were fit to the regular solution model, Equation 1:

$$\chi_M T = (\chi_M T)_{min} + \frac{(\chi_M T)_{max} - (\chi_M T)_{min}}{1 + e^{\frac{\Delta S(T_c)}{R(T-1)}}} \quad (1)$$

Where $(\chi_M T)_{min}$ and $(\chi_M T)_{max}$ are the minimum and maximum values of $\chi_M T$ respectively, R is the ideal gas constant with a value of 8.314 J K mol⁻¹. A value of $(\chi_M T)_{max} = 3.17$ cm³ K mol⁻¹ was obtained for the most complete curve in DCE and this value was fixed in fitting the partial transitions in MeCN and DCM. The $(\chi_M T)_{min}$ values (Table S3) are larger than expected for a diamagnetic LS-Co(III)-cat complex while similar to the $\chi_M T$ values 0.13-0.34 cm³ K mol⁻¹ for magnetic data on the solid **1(PF₆)·1.2tol** below 270 K. The large $(\chi_M T)_{min}$ is partially attributed to large TIP contributions because of the low-lying, thermally accessible HS-Co(II)-sq states.

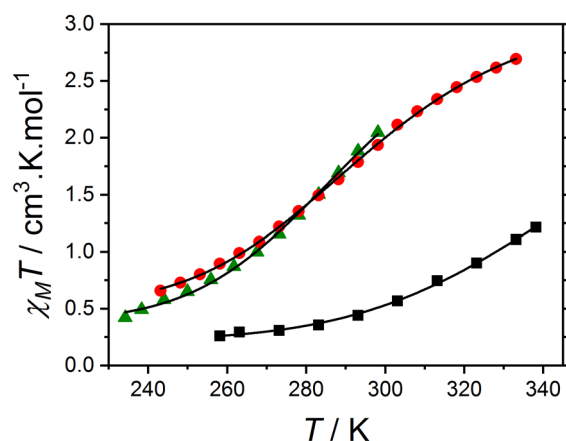


Figure 6. Plot of $\chi_M T$ versus T for 1^+ in MeCN solution (black squares), DCM solution (green triangles) and DCE solution (red circles). Solid black lines indicate fits to the regular solution model with parameters in Table 4.

Table 4. Fitting of Evans method data to regular solution model⁸²

Solvent	T_c / K	ΔS / J K mol ⁻¹	ΔH / kJ mol ⁻¹
DCE	295 ± 1	109 ± 4	32 ± 1
DCM	291 ± 1	121 ± 4	35 ± 1
MeCN	359 ± 1	90 ± 4	32 ± 1

The VT interconversion in solution for 1^+ is confirmed to be solvent-tunable with the trend in transition temperatures: MeCN > DCE > DCM, which confirms observations from UV-Vis data. Entropy and enthalpy parameters of 90-121 J K⁻¹ mol⁻¹ and 32-35 kJ mol⁻¹ are similar to 125 J K⁻¹ mol⁻¹ and 31.2 kJ mol⁻¹ respectively as reported for [Co(Me₃tpa)(Cl₄diox)]⁺ in DCM. The thermodynamic parameters are also within the range of typical values for cobalt-dioxolene VT: $\Delta S = 80$ -150 J K⁻¹ mol⁻¹ and $\Delta H = 20$ -60 kJ mol⁻¹.^{1, 83} The more shallow curve in DCE compared to DCM reveals the solvent dependence of the entropy, in contradiction to

the analogous transition in an iron-dioxolene complex for which ΔS varies by less than $7 \text{ J K}^{-1} \text{ mol}^{-1}$.⁷⁸ The solvent dependence of ΔS may be associated with specific solvent-complex interactions that differ between the two valence tautomers as evident from UV-Vis results.

The literature ΔH values, which were used to benchmark DFT results, were obtained from experimental values of $\Delta G_{[T=298 \text{ K}]}$ using electrochemical data, under the assumption of a $\Delta S = 50 \text{ J K}^{-1} \text{ mol}^{-1}$, smaller than those experimentally determined by monitoring the interconversion as a function of temperature, and were thus underestimated.^{7, 11} In this respect the deviation between experimental and calculated ΔH values is apparently systematic. However, in the present case, DFT calculations can correctly predict the trends in ΔH to identify target VT complex $\mathbf{1}^+$, which was predicted to have T_c around room temperature. Solution magnetic susceptibility data and UV-Vis absorption spectroscopy confirm that $\mathbf{1}^+$ displays VT in solution with critical temperatures in the range 291-359 K.

Electrochemistry. Cyclic voltammograms were measured for DMF solutions of $\mathbf{1}$, $\mathbf{1-Zn}$ and $\mathbf{1}^+$ using a glassy carbon electrode (Figure 7). All potentials are referenced to the ferrocene/ferrocenium couple using ferrocene measured immediately afterwards. The tabulated (Table 5) midpoint potentials (E_m) are calculated by taking the average of the anodic and cathodic peak potentials (E_p). Reversible processes are identified by peak-to-peak separations (ΔE_p) close to the value of 71 mV measured under the same conditions for ferrocene at a scan rate of 100 mV s^{-1} .

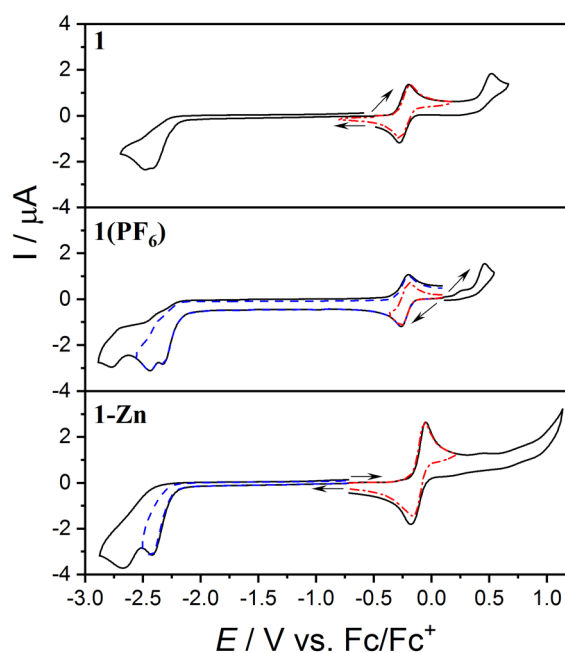


Figure 7. Cyclic voltammetry of N,N'-dimethylformamide (DMF) solutions (1.0 mM with 0.1 M Bu₄NPF₆) of compound **1** (top), **1(PF₆)** (middle) and **1-Zn** (bottom) obtained with a 1.0 mm diameter glassy carbon electrode at a scan rate of 100 mV.s⁻¹. The blue dashed and red dot-dashed lines plot the voltammograms measured with a switching potential immediately past the first reversible process or highly negative reduction respectively. Arrows indicate the direction of the scan.

Table 5. Cyclic voltammetry data for cobalt and zinc complexes (1.0 mM in DMF with 0.1 M Bu₄NPF₆)^a

	E_{pc} / V^b	E_{pc} / V^b	E_{pc} / V^b	E_m / V	E_{pa} / V^b
				($\Delta E_p / \text{mV}$)	
1		-2.48	-2.42	-0.22 (95)	0.52
1⁺	-2.77	-2.44	-2.33	-0.23 (68)	0.46
1-Zn		-2.67	-2.43	-0.11 (101)	

^a Potentials reported versus Fc/Fc⁺ couple.

^b Anodic and cathodic peak potentials are reported at 100 mV s⁻¹ scan rates.

A redox process is observed at -0.22/-0.23 V as an oxidation of **1** and a reduction of **1**⁺. The process appears to be reversible for **1**⁺ and quasi-reversible for **1** with $\Delta E_p = 68$ and 95 mV respectively. Compound **1-Zn** displays the first oxidation at a higher potential of -0.11 V which appears quasi-reversible with $\Delta E_p = 101$ mV. An irreversible oxidation is observed for **1** at +0.52 V and **1**⁺ at +0.46 V but no oxidation is observed at higher potentials for **1-Zn**. At highly negative potentials, multiple irreversible reduction processes are observed in **1**, **1**⁺ and **1-Zn**.

The charge distribution of **1**⁺ in DMF solution at room temperature is Co(III)-cat (see UV-Vis spectroscopy section), while **1** exists as Co(II)-cat. The charge distributions of **1**⁺ and **1** imply that the first reduction of **1**⁺ at -0.22 V is a metal-based reduction of Co(III) to Co(II). Both ligand and metal oxidations of **1** are possible. The ligand-based oxidation of tetrabromocatecholate to tetrabromosemiquinonate (Br₄sq⁻) with a divalent metal can be expected to occur around -0.11 V as observed for **1-Zn**. As the first oxidation of **1** occurs a very similar potential to the first reduction of **1**⁺, this oxidation is assigned as the metal-based oxidation of Co(II)-cat to Co(III)-cat. The first oxidation of **1** occurs at a potential slightly more negative than the ferrocenium/ferrocene couple, suggesting that **1**⁺ would be accessible by chemical oxidation of **1** using ferrocenium, which proved to be correct. Based on the charge distribution of **1**⁺ in DMF, the first oxidation of **1**⁺ and second oxidation of **1** are assigned to an irreversible ligand-based oxidation of Co(III)-Br₄cat to Co(III)-Br₄sq. The identity of these reductions is confirmed by examining the DFT spin densities of the lowest energy states of **1**, **1**⁺, **1**²⁺, **1-Zn** and **1-Zn**⁺ after geometry optimization using the OPBE/TZP/ZORA/COSMO method with DMF as the solvent. The reductions observed for **1**, **1-Zn** and **1**⁺ at very negative potentials may correspond to Me₃tpa-based reductions but cannot be unambiguously assigned.

For a candidate VT system, the separation between the midpoint potentials of the (reversible) first 1e-oxidation and 1e-reduction may be defined as Δ_{ox-red} (Equations S1-S9). For complex **1**⁺, Δ_{ox-red} is cannot be accurately determined due to the irreversibility of process

II, but can be estimated as approximately 690 mV based on the peak potential at a scan rate of 100 mV s⁻¹. In the case where one of these redox processes is metal-based and the other ligand-based, we propose Δ_{ox-red} to give an indication of the accessibility of the VT transition. The Δ_{ox-red} parameter has the advantage that both processes are observed for a single complex, in contrast to literature methods to measure ΔG for the VT interconversion which require measurements on the VT complex and a structural analogue with another metal (Equations S10-S11).^{7, 84} Comparison of Δ_{ox-red} values for which the solution VT and electrochemistry are well characterized (Table 6) allow us to propose that a value of Δ_{ox-red} less than ~740 mV is a good indicator of the possibility for VT. There are some contradictory examples, but this value is consistent with related cobalt-bis(dioxolene) systems with potential separations of greater than 800 mV that display temperature-invariant redox states and no VT transition up to room temperature.^{68, 85} In principle, electrochemical data for any parent complex with metal and ligand redox-activity can also provide insight into the possibility of VT in the oxidized or reduced form. In the present work, the separation of 740 mV between processes *I* and *II* of non-VT complex **1** foreshadows VT in **1**⁺.

Table 6. Electrochemical data for selected solution VT complexes

Complex	Δ_{ox-red} / mV ^a	Metal	Ligand	Solvent	VT range / K	Method	Ref
[Ni(<i>t</i> Bu-salcn)]	340	Ni(II/III)	phenolate-/phenoxyl•	DCM	123-193	EPR	86
[Ni(<i>t</i> Bu-salen)]	460	Ni(II/III)	phenolate-/phenoxyl•	DCM	4-260	EPR	87
[Co(<i>t</i> meda)(cat)(sq)]	670	Co(II/III)	3,6- <i>t</i> Bu ₂ cat ²⁻ /3,6- <i>t</i> Bu ₂ sq ^{•-}	DMF	248-353	UV-Vis	88
[Co(Me ₃ tpa)(Br ₄ diox)](PF ₆)	690 ^b	Co(II/III)	Br ₄ cat ²⁻ /Br ₄ sq ^{•-}	DMF	234-338	Evans method	This work
[Co(bis-amido-py)] ⁺	710	Co(I/II)	pyridine/pyridine ^{•-}	MeCN	298	RT UV-Vis-NIR	89
<i>cis</i> -[Os(^{OX} L)(PPh ₃)Br ₂]	710	Os(II/III)	phenolate-/phenoxyl•	DCM	115-295	EPR	90
[{Co(Me ₂ tpa)} ₂ (spiro)](ClO ₄) ₂	715 ^{b,c}	Co(II/III)	cat ²⁻ /sq ^{•-}	MeCN	170-300	UV-Vis	68
[Cu(bis-guanidino)Cl ₂](PF ₆)	740 ^b	Cu(I/II)	guanidino ^{+•} /guanidino ²⁺	DCM	193-303	NMR	91
[Fe(bispicen)(Cl ₄ diox) ₂]-DMF	1110	Fe(II/III)	Cl ₄ cat ²⁻ /Cl ₄ sq ^{•-}	DMF	338-298	Vis-NIR	85

^a Δ_{ox-red} is defined as the separation between the 1e-oxidation and 1e-reduction midpoint potentials as defined above ^b Δ_{ox-red} is calculated using E_{pa} as oxidation process is irreversible, scan rate 100 mV s⁻¹. ^c First reduction of bis(dioxolene) ligand

CONCLUDING REMARKS

In this work we have identified an accurate DFT method for predicting valence tautomerism in the family of complexes [Co(Me_{*n*}tpa)(X_{*d*}diox)]⁺ using the OPBE functional and relativistic TZP basis set with relativistic and solvent corrections. It is evident that explicit consideration of all substituents on the redox-active ligand is necessary for accurate spin state energetics, and we recommend that all electronically-active substituents, especially *tert*-butyl groups, not be excluded by default. Using the identified DFT method, a VT transition was predicted for complex **1**⁺ and this prediction was validated following synthesis and experimental investigation of **1**(PF₆) and **1**(BPh₄) by variable temperature magnetic susceptibility, Evans method and UV-visible absorption spectroscopy measurements. Compound **1**(BPh₄) and **1**(PF₆) display incomplete VT interconversions in the solid state, which is irreversible for **1**(BPh₄). In solution, complex **1**⁺ undergoes solvent-tunable thermally induced VT transitions

with T_c of 291, 295 and 359 K in DCM, DCE and MeCN respectively. We also propose a convenient electrochemistry-based experimental predictor for the likelihood of a VT transition as a separation between the half-potentials of the relevant redox-processes as less than ~ 740 mV.

Calculations of spin-state energies in valence tautomeric complexes face all the challenges of modelling spin crossover with the added complications of changes in metal and ligand oxidation states. The most accurate DFT methods for SCO and VT use similar functionals in OPBE, B3LYP* and TPSSh, and similar energetic corrections, but the theory is more advanced for SCO in terms of validating methods over multiple metals and oxidation states, considering crystal packing effects and moving towards the prediction of critical temperatures.^{29, 55, 92} The systematic study reported herein has allowed elucidation of a DFT method that is suitable for prediction of compounds likely to undergo a valence tautomeric transition. The method was benchmarked with existing experimental data and successfully used to predict a VT interconversion in a previously unreported complex. This computational method now provides a powerful tool for accessing compounds with properties desirable for new technologies, allowing efficient design of new molecular materials. In this respect we foresee the application of this methodology to other families of compounds in the near future.

EXPERIMENTAL SECTION

DFT Method. All density-functional calculations were carried out using the Amsterdam Density Functional (ADF 2014) package with default convergence parameters for the self-consistent field procedure (energy: $1e-3$ Hartree) and geometry optimization (gradient: $1e-3$ Hartree/Å; coordinates: $1e-2$ Å).⁹³⁻⁹⁵ Independent optimizations of both spin states LS-Co(III)-cat (spin restricted) and HS-Co(II)-sq (spin unrestricted) were performed. Initial geometry optimizations to identify the lowest energy geometric isomers were performed with the

computationally inexpensive GGA functional BP86 and triple-zeta basis sets with one polarization function (TZP) on all elements (see S.I.-8 in supporting information).^{16-17, 56} All further calculations were performed with full geometry optimization using solvation effects (COSMO), relativistic effects (ZORA) and relativistically contracted TZP basis sets on all atoms.⁵⁶⁻⁶⁰ Functional screening calculations for determining ΔH used MeCN as the solvent to compare with enthalpy values in MeCN.⁵⁷⁻⁶⁰ Calculations of ΔH for the entire family of complexes and **1** were performed with the GGA functional OPBE, and additionally included a vibrational analysis in each spin state. The calculation of ΔH was repeated with DCM solvation for selected complexes. The OPBE/TZP/ZORA/COSMO method was used with DMF as the solvent to perform calculations on **1**, **1**⁺, **1**²⁺, **1-Zn** and **1-Zn**⁺ and identify the charge distributions in electrochemical measurements. Calculations were performed in C_1 symmetry unless C_S symmetry is stated. Additional details are available in the Supporting Information, S.I.-8, S.I.-9 and S.I.-10.

Synthesis. Materials and Methods. Synthesis of **1** was performed in atmospheric conditions with solvents used as received. Syntheses of **1(PF₆)** and **1(BPh₄)** were performed in a nitrogen atmosphere with exclusion of oxygen and moisture using Schlenk techniques. Solvents were dried over 3 Å sieves and degassed with a minimum of three freeze-pump-thaw cycles before use. All chemicals were of reagent grade and used as received. Tris(6-methyl-2-pyridylmethyl)amine (Me₃tpa) was synthesized based on a literature procedure with recrystallisation from diethyl ether.⁷ Compound 6-methyl-2-aminomethylpyridine and the precursor 6-formaldoximo-2-methylpyridine were synthesized from literature procedures.⁹⁶⁻⁹⁷ Ferrocenium tetraphenylborate was synthesized according to literature procedures and stored at -25 °C under nitrogen.⁹⁸

[Co(Me₃tpa)(Br₄cat)] (**1**). *Caution!* Perchlorate salts in contact with organic material are potentially explosive and should not be heated or allowed to become dry. Handle in small

quantities with sufficient care.⁹⁹ Cobalt perchlorate can alternatively be substituted with $\text{CoCl}_2 \cdot 6\text{H}_2\text{O}$. Tris(6-methyl-2-pyridylmethyl)amine (Me_3tpa , 0.229 g, 0.869 mmol) was added to a solution of $\text{Co}(\text{ClO}_4)_2 \cdot 6\text{H}_2\text{O}$ (0.320 g, 0.874 mmol) in methanol (20 mL). After 10 minutes of stirring at room temperature, a solution of tetrabromocatechol (Br_4catH_2 , 0.371 g, 0.871 mmol) in methanol (40 mL), deprotonated with triethylamine (0.243 mL, 0.871 mmol), was added dropwise. The precipitate was collected by vacuum filtration, washed with methanol, diethyl ether and air dried to give $[\text{Co}(\text{Me}_3\text{tpa})(\text{Br}_4\text{cat})]$ as a red solid (Yield: 0.668 g, 94%). Single crystals of X-ray diffraction quality were produced by layering a DMF solution with diethyl ether (1:2). A microcrystalline bulk sample was produced by diluting a hot DMF solution of the crude product with diethyl ether (1:2), collecting the resultant precipitate by vacuum filtration, washing with diethyl ether and air drying. Anal. Calcd for $\text{C}_{27}\text{H}_{24}\text{N}_4\text{O}_2\text{Br}_4\text{Co}$: C, 39.79; H, 2.79; N, 6.87. Found: C, 40.08; H, 3.03; N, 6.86. HR-MS (ESI-QTOF) m/z $[\text{M}]^+$ Calcd for $\text{C}_{27}\text{H}_{24}\text{N}_4\text{O}_2\text{Br}_4\text{Co}$ 814.7924; Found 814.7831. TGA data are consistent with no solvation (Figure S1). Selected IR data (KBr, cm^{-1}): 1604 (m), 1577 (m), 1498 (w), 1467 (s), 1446 (s), 1398 (w), 1385 (w), 1367 (w), 1348 (w), 1258 (m), 1164 (w), 1122 (w), 1097 (w), 1040 (w), 1007 (w), 975 (w), 914 (w), 888 (w), 787 (m), 733 (m), 608 (w), 562 (w), 513 (w).

$[\text{Zn}(\text{Me}_3\text{tpa})(\text{Br}_4\text{cat})]$, (**1-Zn**). Synthesized as per **1** from Me_3tpa (0.216 g, 0.651 mmol), Br_4catH_2 (0.277 g, 0.650 mmol) and triethylamine (0.181 mL, 1.30 mmol). The reagent $\text{Co}(\text{ClO}_4)_2 \cdot 6\text{H}_2\text{O}$ was replaced by ZnCl_2 (0.0903 g, 0.663 mmol) in **1-Zn**. A larger volume of methanol was used to account for the low solubility of ZnCl_2 . Compound **1-Zn** was obtained as a microcrystalline yellow powder (Yield: 0.336 g, 63%). Anal. Calcd for $\text{C}_{27}\text{H}_{24}\text{N}_4\text{O}_2\text{Br}_4\text{Zn}$: C, 39.47; H, 2.94; N, 6.82. Found: C, 39.76; H, 2.67; N, 6.89. HR-MS (ESI-QTOF) m/z $[\text{M}+\text{H}]^+$ Calcd for $\text{C}_{27}\text{H}_{25}\text{N}_4\text{O}_2\text{Br}_4\text{Zn}$ 822.7944; Found 822.7823. Selected IR data (KBr, cm^{-1}): 1603 (m), 1578 (m), 1501 (w), 1473 (s), 1447 (s), 1396 (w), 1385 (w), 1366 (w), 1353 (w),

1254 (m), 1222 (w), 1163 (w), 1127 (w), 1117 (w), 1095 (w), 1041 (w), 1008 (w), 975 (w), 928 (w), 915 (w), 889 (w), 787 (m), 735 (m), 615 (w), 567 (w), 523 (w).

[Co(Me₃tpa)(Br₄diox)](PF₆)·1.2C₆H₅CH₃ (1(PF₆)·1.2tol). A filtered solution of ferrocenium hexafluorophosphate (0.145 g, 0.437 mmol) in DMF was slowly added to **1** (0.356 g, 0.437 mmol) in DMF (500 mL total) and stirred at room temperature overnight. The solvent was removed under reduced pressure on the Schlenk line, taking care not to heat the solution above 45 °C. The residue was rinsed with diethyl ether (5 × 50 mL) until the filtrate was clear. The residue was taken up in methanol (100 mL), filtered and the solvent was removed under reduced pressure. The crude product was recrystallized from 75 °C toluene (4 × 100 mL) with hot filtration and cooling slowly in an oil bath overnight obtain pink-brown needle crystals. The crystalline product was collected by vacuum filtration, dried under a blanket of nitrogen and stored under atmospheric conditions (Yield: 72.7 mg, 15%). Anal. Calcd for C_{35.4}H_{33.6}N₄O₂Br₄CoPF₆: C, 39.56; H, 3.15; N, 5.21. Found C, 39.90; H, 3.33; N, 5.22. HR-MS (ESI-QTOF) m/z Calcd for [M-PF₆-1.2tol]⁺, C₂₇H₂₄N₄O₂Br₄Co 814.7924; Found 814.7928. TGA data show the onset of desolvation at 90 °C and are consistent with 1.2 toluene solvate per molecule, lost over two steps centered at 99 and 129 °C (Figure S1). Selected IR data (KBr, cm⁻¹): 1612 (m), 1578 (w), 1512 (w), 1494 (w), 1472 (w), 1445 (s), 1398 (w), 1385 (w), 1356 (w), 1346 (w), 1272 (m), 1233 (m), 1215 (w), 1172 (w), 1121 (w), 1102 (w), 1083 (w), 1040 (w), 1018 (w), 999 (w), 968 (w), 943 (w), 920 (w), 868 (w), 841 (s), 787 (m), 768 (w), 746 (m), 698 (w), 623 (w), 586 (w), 558 (m), 519 (w), 501 (w), 468 (w), 443 (w).

[Co(Me₃tpa)(Br₄diox)](BPh₄) (1(BPh₄)). A suspension of [Co(Me₃tpa)(Br₄cat)] (0.269 g, 0.330 mmol) and ferrocenium tetraphenylborate (0.167 g, 0.330 mmol) in isopropanol (40 mL) was sonicated for 1.5 h. The product was collected by vacuum filtration, washed with isopropanol (3 × 10 mL), air dried and stored under atmospheric conditions (Yield: 0.362 g, 97%). Single crystals suitable for X-ray diffraction were obtained from vapor diffusion of an

acetone solution with hexane. The bulk sample was recrystallized from the layering of a DCM solution with diethyl ether (4:1:4 DCM:50/50 DCM/Et₂O:Et₂O) to obtain **1(BPh₄)** as fine light brown needles (61% recovery). Anal. Calcd for C₅₁H₄₄N₄O₂Br₄CoB: C, 54.00; H, 3.91; N, 4.94. Found C, 53.66; H, 3.85; N, 4.94. HR-MS (ESI-QTOF) m/z Calcd for [M-BPh₄]⁺, C₂₇H₂₄N₄O₂Br₄Co 814.7924; Found 814.7911. TGA data show no evidence of solvent loss (Figure S1). Selected IR data (KBr, cm⁻¹): 1601 (m), 1577 (m), 1512 (w), 1471 (w), 1445 (s), 1393 (w), 1385 (w), 1355 (w), 1274 (m), 1235 (m), 1170 (w), 1151 (w), 1133 (w), 1118 (w), 1102 (w), 1066 (w), 1033 (w), 1018 (w), 998 (w), 966 (w), 938 (w), 919 (w), 889 (w), 844 (w), 785 (m), 768 (w), 745 (m), 735 (w), 707 (m), 623 (w), 612 (m), 587 (w), 567 (w), 560 (w), 542 (w), 519 (w), 501 (w), 476 (w), 468 (w), 444 (w).

X-ray Data Collection and Structure Solution. Single crystal X-ray diffraction data (Table S1) of **1** and **1-Zn** were collected at 130 K using a Rigaku Oxford Diffraction SuperNova Dual Wavelength Diffractometer with mirror monochromated Cu-K α radiation (λ = 1.5418 Å). Data for **1(BPh₄)** and **1(PF₆)·2tol** (Tables S1 and S2) were collected at the MX1 beamline at the Australian Synchrotron, using radiation tuned to approximately Mo-K α radiation (λ = 0.7108 Å), fitted with a silicon double crystal monochromator and Oxford Instruments CryoJet 5 cryostat.¹⁰⁰ Datasets were collected at 100, 200, 250, 275, 300, 315, 330 and 380 K for **1(PF₆)·2tol** with the sample losing crystallinity by 400 K. The structure of **1(BPh₄)** was collected at 100 K; there was an increase in disorder on rising temperature which precluded the observation of a transition.

Crystals were transferred directly from the mother liquor into a cryoprotective oil to prevent solvent loss. Three single crystals were used for variable temperature runs (100–275 K, 300–330 K and 380 K) on **1(PF₆)·2tol**, as crystals suffered significant radiation damage if used for more than 3-4 full collections. The data of **1** and **1-Zn** were processed using CrysAlisPro,¹⁰¹ while data reduction for **1(PF₆)·2tol** and **1(BPh₄)** were performed with XDS,¹⁰²

using moderate multi-scan absorption correction in SADABS.¹⁰³ All structures were solved using the intrinsic phasing routine in SHELXT and refined using a full-matrix least square procedure based upon F^2 using SHELXL within OLEX2.¹⁰⁴⁻¹⁰⁶ The positions of all non-hydrogen atoms were refined using anisotropic displacement factors. Hydrogen atoms were placed geometrically, and their positions were constrained to geometrical estimates using the riding model. One of the toluene molecules in **1**(PF₆)·2tol was disordered over two positions and refinement was carried out with both components being constrained to ideal geometry. As the temperature increased the disorder and thermal motion of both toluene molecules increased requiring more restraints/constraints to maintain the geometry and displacement parameters of the atoms of both solvent molecules to chemically sensible values.

X-ray powder diffraction data were measured on a Rigaku Oxford Diffraction SuperNova Dual Wavelength single crystal X-ray diffractometer using Cu-K α radiation at 130 K. Powder samples were prepared by crushing the samples gently and loading in a glass capillary for measurement. Data were collected to $2\theta = 80^\circ$ with an exposure time of 60 s per frame and processed using CrysAlisPro.¹⁰¹

Electrochemistry. Electrochemical measurements were performed in *N,N'*-dimethylformamide at room temperature using a standard three-electrode configuration connected to an eDAQ computer-controlled potentiostat. Measurements were performed under a continuous nitrogen flow. The three-electrode system consisted of a 1.0 mm diameter glassy carbon electrode (Cypress Systems), a platinum wire auxiliary electrode and a commercially available Ag/AgCl reference electrode (eDAQ). Analyte solutions of 1 mM were prepared in solvent containing 0.1 M Bu₄NPF₆ as the supporting electrolyte. All potentials have been referenced *versus* the ferrocene/ferrocenium redox couple, measured immediately afterwards.

Solid-State Magnetic Measurements. Magnetic measurements were performed on a Quantum Design MPMS SQUID magnetometer using a scan rate of 0.7 K min⁻¹ with

microcrystalline samples restrained by pressing into pellets with polytetrafluoroethylene (PTFE) tape. Measurements were corrected for the diamagnetic contribution of the PTFE tape and diamagnetic contribution of the samples using Pascal's constants.¹⁰⁷

Solution-Based Magnetic Measurements. Solution-based magnetic susceptibility measurements of **1(PF₆)** were measured in MeCN (258-338 K), DCM (234-298 K) and DCE (243-333 K) by ¹H NMR spectroscopy according to Evans method.⁸⁰ Measurements were recorded on an Agilent DD2 500 MHz spectrometer (MeCN) and Bruker Ascend 500 MHz spectrometer (DCM and DCE). A solvent mixture was prepared containing deuterated solvent and 0.5-2% *t*BuOH as a standard. The compound **1(PF₆)** was dissolved in the solvent mixture to form a solution of precisely known concentration (2.00 mM in *d*₃-MeCN, 2.35 mM in *d*₂-DCM, 2.57 mM in *d*₂-DCE) and placed in an NMR tube. A narrow capillary or co-axial NMR tube (for DCM) was filled with the solvent mixture and placed inside the NMR tube as an internal reference. The shift of the *t*BuOH singlet in the paramagnetic solution compared to *t*BuOH in the internal reference, $\Delta\nu$ in Hz, can be used to calculate the mass susceptibility of the compound, χ_g , according to Equation 2.

$$\chi_g = \frac{3\Delta\nu}{4\pi m\nu} + \chi_0 + \chi_0 \frac{d_0 - d_s}{m} \quad (2)$$

Where m is the concentration of the paramagnetic solution in g cm⁻³, corrected for the temperature dependence of the density of the solvent,¹⁰⁸⁻¹¹⁰ ν is the spectrometer frequency in Hz, χ_0 is the mass susceptibility of the solvent mixture, d_0 is the density of the pure solvent mixture and d_s is the density of the compound solution. As the solution was dilute the following approximation can be made: $d_s = d_0 + m$, resulting in the cancellation of the second and third terms of Equation 2. The mass susceptibility was converted to the molar susceptibility by

multiplying by the molecular weight and then corrected for the diamagnetic contribution of the compound using Pascal's constants.¹⁰⁷

Other Measurements. Elemental analyses were performed by the Campbell Microanalytical Laboratory, Chemistry Department, University of Otago, New Zealand. High resolution mass spectra (HR-MS) were performed on an Agilent 6520 Accurate-Mass Q-TOF spectrometer. Thermogravimetric analyses were performed on a Mettler Toledo thermal analyzer using ramp rates of 5 or 7 °C min⁻¹ up to a maximum temperature of 400 °C. Temperature dependent ultraviolet-visible (UV-Vis) absorption spectra recorded on an Agilent Cary 60 UV-Vis spectrophotometer fitted with a Single Cell Peltier Accessory in the range 340-1000 nm. Spectra were recorded in 5 K intervals in the range 283-348 K. Infrared spectra (KBr disk) were recorded on a Bruker Tensor 27 FTIR spectrometer.

ASSOCIATED CONTENT

Supporting Information. The supporting information is available free of charge online: Additional TGA, IR, crystallographic and structural data, powder X-ray diffraction, fitting parameters, electrochemistry and DFT computational details (PDF). X-ray crystallographic files in CIF format for **1**, **1-Zn**, **1(PF₆)·2tol** (100, 200, 250, 275, 300, 315, 330, 380 K) and **1(BPh₄)** (CIF). CCDC1878624-1878634 contains all crystallographic data. Optimized coordinates of all DFT structures (ZIP file of XYZ files).

AUTHOR INFORMATION

Corresponding Author

*Email: c.boskovic@unimelb.edu.au

Author Contributions

The manuscript was written through contributions of all authors. All authors have given approval to the final version of the manuscript.

Notes

The authors declare no competing financial interest.

ACKNOWLEDGMENTS

We thank the Australian Research Council for financial support (DP150100353) to CB and LS. GKG acknowledges the support of an Elizabeth and Vernon Puzey Scholarship from the University of Melbourne and an Australian Government Research Training Award. LS and MEB acknowledge the financial support from Italian MUIR through Project No. PRIN 2015-HYFSRT. Part of this research was undertaken on the MX1 beamline at the Australian Synchrotron, Victoria, Australia.

REFERENCES

1. Tezgerevska, T.; Alley, K. G.; Boskovic, C., Valence tautomerism in metal complexes: Stimulated and reversible intramolecular electron transfer between metal centers and organic ligands. *Coord. Chem. Rev.* **2014**, *268*, 23-40.
2. Caneschi, A.; Dei, A.; Fabrizi de Biani, F.; Gütllich, P.; Ksenofontov, V.; Levchenko, G.; Hofer, A.; Renz, F., Pressure- and temperature-induced valence tautomeric interconversion in a *o*-dioxolene adduct of a cobalt - tetraazamacrocyclic complex. *Chem. - Eur. J.* **2001**, *7*, 3926-3930.
3. Yokoyama, T.; Okamoto, K.; Nagai, K.; Ohta, T.; Hayami, S.; Gu, Z.-Z.; Nakajima, R.; Sato, O., Photo-induced magnetized state of Co(DTBSQ)(DTBCat)(phen).C₆H₅CH₃ studied by X-ray absorption spectroscopy. *Chem. Phys. Lett.* **2001**, *345*, 272-276.
4. Markevtsev, I. N.; Monakhov, M. P.; Platonov, V. V.; Mischenko, A. S.; Zvezdin, A. K.; Bubnov, M. P.; Abakumov, G. A.; Cherkasov, V. K., Field-induced spin phase transition in a Co complex. *J. Magn. Magn. Mater.* **2006**, *300*, e407-e410.
5. Droghetti, A.; Sanvito, S., Electric Field Control of Valence Tautomeric Interconversion in Cobalt Dioxolene. *Phys. Rev. Lett.* **2011**, *107*, 047201/1-047201/4.
6. Poneti, G.; Mannini, M.; Sorace, L.; Sainctavit, P.; Arrio, M.-A.; Otero, E.; Criginski Cezar, J.; Dei, A., Soft-X-ray-Induced Redox Isomerism in a Cobalt Dioxolene Complex. *Angew. Chem. Int. Ed.* **2010**, *49*, 1954-1957.
7. Beni, A.; Dei, A.; Laschi, S.; Rizzitano, M.; Sorace, L., Tuning the charge distribution and photoswitchable properties of cobalt-dioxolene complexes by using molecular technique. *Chem. - Eur. J.* **2008**, *14*, 1804-1813.

8. Calzolari, A.; Chen, Y.; Lewis, G. F.; Dougherty, D. B.; Shultz, D.; Buongiorno Nardelli, M., Complex Materials for Molecular Spintronics Applications: Cobalt Bis(dioxolene) Valence Tautomers, from Molecules to Polymers. *J. Phys. Chem. B* **2012**, *116*, 13141-13148.
9. Senthil Kumar, K.; Ruben, M., Emerging trends in spin crossover (SCO) based functional materials and devices. *Coord. Chem. Rev.* **2017**, *346*, 176-205.
10. Létard, J.-F.; Guionneau, P.; Goux-Capes, L., Towards Spin Crossover Applications. In *Spin Crossover in Transition Metal Compounds*, Springer: Berlin, Heidelberg, 2004; Vol. 235, pp 221-249.
11. Dei, A.; Feis, A.; Poneti, G.; Sorace, L., Thermodynamics of valence tautomeric interconversion in a tetrachlorodioxolene:cobalt 1:1 adduct. *Inorg. Chim. Acta* **2008**, *361*, 3842-3846.
12. Bencini, A.; Caneschi, A.; Carbonera, C.; Dei, A.; Gatteschi, D.; Righini, R.; Sangregorio, C.; van Slageren, J., Tuning the physical properties of a metal complex by molecular techniques: the design and the synthesis of the simplest cobalt-*o*-dioxolene complex undergoing valence tautomerism. *J. Mol. Struct.* **2003**, *656*, 141-154.
13. Dapporto, P.; Dei, A.; Poneti, G.; Sorace, L., Complete direct and reverse optically induced valence tautomeric interconversion in a cobalt-dioxolene complex. *Chem. - Eur. J.* **2008**, *14*, 10915-10918.
14. Deeth, R. J.; Handley, C. M.; Houghton, B. J., Theoretical Prediction of Spin-Crossover at the Molecular Level. In *Spin-Crossover Materials: Properties and Applications*, Halcrow, M. A., Ed. John Wiley & Sons, Ltd.: 2013.

15. Neese, F., Prediction of molecular properties and molecular spectroscopy with density functional theory: From fundamental theory to exchange-coupling. *Coord. Chem. Rev.* **2009**, *253*, 526-563.
16. Becke, A. D., Density-functional exchange-energy approximation with correct asymptotic behavior. *Phys. Rev. A* **1988**, *38*, 3098-3100.
17. Perdew, J. P., Density-functional approximation for the correlation energy of the inhomogeneous electron gas. *Phys. Rev. B* **1986**, *33*, 8822-8824.
18. Becke, A. D., Density-functional thermochemistry. III. The role of exact exchange. *J. Chem. Phys.* **1993**, *98*, 5648-5652.
19. Paulsen, H.; Schüenemann, V.; Wolny, J. A., Progress in Electronic Structure Calculations on Spin-Crossover Complexes. *Eur. J. Inorg. Chem.* **2013**, *2013*, 628-641.
20. Reiher, M.; Salomon, O.; Artur Hess, B., Reparameterization of hybrid functionals based on energy differences of states of different multiplicity. *Theor. Chem. Acc.* **2001**, *107*, 48-55.
21. Reiher, M., Theoretical Study of the Fe(phen)₂(NCS)₂ Spin-Crossover Complex with Reparametrized Density Functionals. *Inorg. Chem.* **2002**, *41*, 6928-6935.
22. Vargas, A.; Krivokapic, I.; Hauser, A.; Lawson Daku, L. M., Towards accurate estimates of the spin-state energetics of spin-crossover complexes within density functional theory: a comparative case study of cobalt(II) complexes. *Phys. Chem. Chem. Phys.* **2013**, *15*, 3752-3763.
23. Perdew, J. P.; Burke, K.; Ernzerhof, M., Generalized Gradient Approximation Made Simple. *Phys. Rev. Lett.* **1996**, *77*, 3865-3868.

24. Handy, N. C.; Cohen, A. J., Left-right correlation energy. *Mol. Phys.* **2001**, *99*, 403-412.
25. Matouzenko, G. S.; Borshch, S. A.; Schuenemann, V.; Wolny, J. A., Ligand strain and conformations in a family of Fe(II) spin crossover hexadentate complexes involving the 2-pyridylmethyl-amino moiety: DFT modelling. *Phys. Chem. Chem. Phys.* **2013**, *15*, 7411-7419.
26. Sato, D.; Shiota, Y.; Juhász, G.; Yoshizawa, K., Theoretical Study of the Mechanism of Valence Tautomerism in Cobalt Complexes. *J. Phys. Chem. A* **2010**, *114*, 12928-12935.
27. Jensen, K. P.; Cirera, J., Accurate Computed Enthalpies of Spin Crossover in Iron and Cobalt Complexes. *J. Phys. Chem. A* **2009**, *113*, 10033-10039.
28. Minkin, V. I.; Starikova, A. A.; Minyaev, R. M., Computational design of valence tautomeric adducts of CoII diketonates with redox-active o-benzoquinone ligands. *Dalton Trans.* **2013**, *42*, 1726-1734.
29. Cirera, J.; Via-Nadal, M.; Ruiz, E., Benchmarking Density Functional Methods for Calculation of State Energies of First Row Spin-Crossover Molecules. *Inorganic Chemistry* **2018**, *57*, 14097-14105.
30. Swart, M., Accurate Spin-State Energies for Iron Complexes. *J. Chem. Theory Comput.* **2008**, *4*, 2057-2066.
31. Siig, O. S.; Kepp, K. P., Iron(II) and Iron(III) Spin Crossover: Toward an Optimal Density Functional. *J. Phys. Chem. A* **2018**, *122*, 4208-4217.
32. Sirirak, J.; Sertphon, D.; Phonsri, W.; Harding, P.; Harding, D. J., Comparison of density functionals for the study of the high spin low spin gap in Fe(III) spin crossover complexes. *Int. J. Quantum Chem.* **2017**, *117*, e25362.

33. Houghton, B. J.; Deeth, R. J., Spin-State Energetics of FeII Complexes - The Continuing Voyage Through the Density Functional Minefield. *Eur. J. Inorg. Chem.* **2014**, *2014*, 4573-4580.
34. Shahbazi-Raz, F.; Adineh, M.; Safari, N.; Zahedi, M., Theoretical calculation and prediction for experimental design to obtain spin crossover complexes. *Int. J. Quantum Chem.* **2016**, *116*, 1179-1186.
35. Conradie, J.; Ghosh, A., DFT calculations on the spin-crossover complex Fe(salen)(NO): a quest for the best functional. *J. Phys. Chem. B* **2007**, *111*, 12621-12624.
36. Gruden-Pavlović, M.; Stepanović, S.; Perić, M.; Güell, M.; Swart, M., A density functional study of the spin state energetics of polypyrazolylborato complexes of first-row transition metals. *Phys. Chem. Chem. Phys.* **2014**, *16*, 14514-14522.
37. Witt, A.; Heinemann, F. W.; Sproules, S.; Khusniyarov, M. M., Modulation of Magnetic Properties at Room Temperature: Coordination-Induced Valence Tautomerism in a Cobalt Dioxolene Complex. *Chem. - Eur. J.* **2014**, *20*, 11149-11162.
38. Antipin, M. Y.; Ivakhnenko, E. P.; Koshchienko, Y. V.; Knyazev, P. A.; Korobov, M. S.; Chernyshev, A. V.; Lyssenko, K. A.; Starikov, A. G.; Minkin, V. I., Adducts of cobalt(II) bis(salicylaldiminates) and redox-active phenoxazin-1-one: synthesis, structure, and magnetic properties. *Russ. Chem. Bull.* **2013**, *62*, 1744-1751.
39. Minkin, V. I.; Starikova, A. A., Molecular design of the valence tautomeric mixed-ligand adducts of CoII diketonates with redox-active ligands. *Mendeleev Commun.* **2015**, *25*, 83-92.

40. Starikov, A. G.; Starikova, A. A.; Minkin, V. I., Adducts of tetracoordinate cobalt(II) complexes and 1-(pyridin-2-yl)methanimine: Computational search for valence tautomeric systems. *Russ. J. Gen. Chem.* **2016**, *86*, 859-864.
41. Starikova, A. A.; Starikov, A. G.; Minkin, V. I., Quantum chemical modeling of pyrene-4,5-dione adducts with cobalt diketonates. *Comput. Theor. Chem.* **2016**, *1076*, 74-80.
42. Starikov, A. G.; Starikova, A. A.; Minkin, V. I., Quantum-chemical study of (Z)-6,8-di-tert-butyl-N-(4-methoxyphenyl)-3-((4-methoxyphenyl)imino)-3H-phenoxazine-2-amine complexation with cobalt bis(chelate)s. *Dokl. Chem.* **2017**, *476*, 215-218.
43. Minkin, V. I.; Starikova, A. A.; Starikov, A. G., Quantum chemical modeling of valence tautomeric adducts of Co^{II} bischelates with pyrene-4,5-diimines. *Russ. Chem. Bull.* **2017**, *66*, 208-221.
44. Ernzerhof, M.; Scuseria, G. E., Assessment of the Perdew–Burke–Ernzerhof exchange–correlation functional. *J. Chem. Phys.* **1999**, *110*, 5029-5036.
45. Adamo, C.; Barone, V., Toward reliable density functional methods without adjustable parameters: The PBE0 model. *J. Chem. Phys.* **1999**, *110*, 6158-6170.
46. Staroverov, V. N.; Scuseria, G. E.; Tao, J.; Perdew, J. P., Comparative assessment of a new nonempirical density functional: Molecules and hydrogen-bonded complexes. *J. Chem. Phys.* **2003**, *119*, 12129-12137.
47. Tao, J.; Perdew, J. P.; Staroverov, V. N.; Scuseria, G. E., Climbing the Density Functional Ladder: Nonempirical Meta--Generalized Gradient Approximation Designed for Molecules and Solids. *Phys. Rev. Lett.* **2003**, *91*, 146401.

48. Tourón Touceda, P.; Mosquera Vázquez, S.; Lima, M.; Lapini, A.; Foggi, P.; Dei, A.; Righini, R., Transient infrared spectroscopy: a new approach to investigate valence tautomerism. *Phys. Chem. Chem. Phys.* **2012**, *14*, 1038-1047.
49. Starikova, A. A.; Chegerev, M. G.; Starikov, A. G.; Minkin, V. I., A DFT computational study of the magnetic behaviour of cobalt dioxolene complexes of tetraazamacrocyclic ligands. *Comput. Theor. Chem.* **2018**, *1124*, 15-22.
50. Graf, M.; Wolmershäuser, G.; Kelm, H.; Demeschko, S.; Meyer, F.; Krüger, H.-J., Temperature-Induced Spin-Transition in a Low-Spin Cobalt(II) Semiquinonate Complex. *Angew. Chem. Int. Ed.* **2010**, *49*, 950-953.
51. Hocking, R. K.; Deeth, R. J.; Hambley, T. W., DFT Study of the Systematic Variations in Metal-Ligand Bond Lengths of Coordination Complexes: The Crucial Role of the Condensed Phase. *Inorg. Chem.* **2007**, *46*, 8238-8244.
52. Cavigliasso, G.; Stranger, R.; McClintock, L. F.; Cheyne, S. E.; Jaffray, P. M.; Baxter, K. E.; Blackman, A. G., A computational study of the electronic structure, bonding, and spectral properties of tripodal tetraamine Co(III) carbonate complexes. *Dalton Trans.* **2008**, 2433-2441.
53. Bencini, A.; Beni, A.; Costantino, F.; Dei, A.; Gatteschi, D.; Sorace, L., The influence of ligand field effects on the magnetic exchange of high-spin Co(II)-semiquinonate complexes. *Dalton Trans.* **2006**, 722-729.
54. Gransbury, G. K.; Boulon, M.-E.; Gable, R. W.; Mole, R. A.; Moubaraki, B.; Murray, K. S.; Sorace, L.; Soncini, A.; Boskovic, C., Single ion anisotropy and exchange coupling in cobalt(II)-radical complexes: insights from magnetic and ab initio studies. *submitted*.

55. Minkin, V. I.; Starikov, A. G.; Starikova, A. A., Computational insight into magnetic behavior and properties of the transition metal complexes with redox-active ligands: a DFT approach. *Pure Appl. Chem.* **2018**, *90*, 811-824.
56. Van Lenthe, E.; Baerends, E. J., Optimized Slater-type basis sets for the elements 1–118. *J. Comput. Chem.* **2003**, *24*, 1142-1156.
57. Van Lenthe, E.; Baerends, E. J.; Snijders, J. G., Relativistic regular two-component Hamiltonians. *J. Chem. Phys.* **1993**, *99*, 4597-4610.
58. Van Lenthe, E.; Baerends, E. J.; Snijders, J. G., Relativistic total energy using regular approximations. *J. Chem. Phys.* **1994**, *101*, 9783-9792.
59. Van Lenthe, E.; Ehlers, A.; Baerends, E. J., Geometry optimizations in the zero order regular approximation for relativistic effects. *J. Chem. Phys.* **1999**, *110*, 8943-8953.
60. Pye, C. C.; Ziegler, T., An implementation of the conductor-like screening model of solvation within the Amsterdam density functional package. *Theor. Chem. Acc.* **1999**, *101*, 396-408.
61. Adams, D. M.; Hendrickson, D. N., Pulsed Laser Photolysis and Thermodynamics Studies of Intramolecular Electron Transfer in Valence Tautomeric Cobalt *o*-Quinone Complexes. *J. Am. Chem. Soc.* **1996**, *118*, 11515-11528.
62. Jung, O.-S.; Pierpont, C. G., Bistability and Low-Energy Electron Transfer in Cobalt Complexes Containing Catecholate and Semiquinone Ligands. *Inorg. Chem.* **1994**, *33*, 2227-35.

63. Pierpont, C. G.; Jung, O.-S., Thermodynamic Parameters for Cobalt-Quinone Electron Transfer and Spin Transition Steps of the $\text{Co}^{\text{III}}(\text{bpy})(3,5\text{-DBSQ})(3,5\text{-DBCat})/\text{Co}^{\text{II}}(\text{bpy})(3,5\text{-DBSQ})_2$ Valence Tautomeric Equilibrium. *Inorg. Chem.* **1995**, *34*, 4281-3.
64. Horner, L.; Geyer, E., Zur Kenntnis der o-Chinone, XXVII: Redoxpotentiale von Brenzcatechin-Derivaten. *Chem. Ber.* **1965**, *98*, 2016-2045.
65. Tezgerevska, T.; Rousset, E.; Gable, R. W.; Jameson, G. N. L.; Sañudo, E. C.; Starikova, A. A.; Boskovic, C., Valence tautomerism versus spin crossover in pyridinophane-cobalt-dioxolene complexes: an experimental and computational study. *in preparation*.
66. Llunell, M.; Casanova, D.; Cirera, J.; Alemany, P.; Alvarez, S. *SHAPE*, 2.1; Universitat de Barcelona: Barcelona, Spain, 2013.
67. Alvarez, S.; Avnir, D.; Llunell, M.; Pinsky, M., Continuous symmetry maps and shape classification. The case of six-coordinated metal compounds. *New J. Chem.* **2002**, *26*, 996-1009.
68. Alley, K. G.; Poneti, G.; Robinson, P. S. D.; Nafady, A.; Moubaraki, B.; Aitken, J. B.; Drew, S. C.; Ritchie, C.; Abrahams, B. F.; Hocking, R. K.; Murray, K. S.; Bond, A. M.; Harris, H. H.; Sorace, L.; Boskovic, C., Redox Activity and Two-Step Valence Tautomerism in a Family of Dinuclear Cobalt Complexes with a Spiroconjugated Bis(dioxolene) Ligand. *J. Am. Chem. Soc.* **2013**, *135*, 8304-8323.
69. Brown, S. N., Metrical Oxidation States of 2-Amidophenoxide and Catecholate Ligands: Structural Signatures of Metal-Ligand π Bonding in Potentially Noninnocent Ligands. *Inorg. Chem.* **2012**, *51*, 1251-1260.
70. Halcrow, M. A., Structure: function relationships in molecular spin-crossover complexes. *Chem. Soc. Rev.* **2011**, *40*, 4119-4142.

71. Panja, A.; Jana, N. C.; Bauzá, A.; Frontera, A.; Mathonière, C., Solvent-Triggered Cis/Trans Isomerism in Cobalt Dioxolene Chemistry: Distinguishing Effects of Packing on Valence Tautomerism. *Inorg. Chem.* **2016**, *55*, 8331-8340.
72. Chen, X.-Y.; Wei, R.-J.; Zheng, L.-S.; Tao, J., Valence Tautomeric Transitions of Three One-Dimensional Cobalt Complexes. *Inorg. Chem.* **2014**, *53*, 13212-13219.
73. Adams, D. M.; Dei, A.; Rheingold, A. L.; Hendrickson, D. N., Bistability in the [Co^{II}(semiquinonate)₂] to [Co^{III}(catecholate)(semiquinonate)] valence-tautomeric conversion. *J. Am. Chem. Soc.* **1993**, *115*, 8221-9.
74. Affronte, M.; Beni, A.; Dei, A.; Sorace, L., Valence tautomerism interconversion triggers transition to stable charge distribution in solid polymeric cobalt-polyoxolene complexes. *Dalton Trans.* **2007**, 5253-5259.
75. Sever, M. J.; Wilker, J. J., Visible absorption spectra of metal–catecholate and metal–tironate complexes. *Dalton Trans.* **2004**, 1061-1072.
76. Banci, L.; Bencini, A.; Benelli, C.; Gatteschi, D.; Zanchini, C., Spectral-structural correlations in high-spin cobalt(II) complexes. In *Structures versus Special Properties*, Springer Berlin Heidelberg: Berlin, Heidelberg, 1982; pp 37-86.
77. Lever, A. B. P., *Inorganic electronic spectroscopy*. Elsevier Pub. Co: Amsterdam, New York [etc.], 1968.
78. Dei, A., Correlations between optical charge transfer energies and electrochemical data: the iron(III)-catecholato system. *Inorg. Chem.* **1993**, *32*, 5730-5733.
79. Caneschi, A.; Dei, A., Valence Tautomerism in a *o*-Benzoquinone Adduct of a Tetraazamacrocyclic Complex of Manganese. *Angew. Chem. Int. Ed.* **1998**, *37*, 3005-3007.

80. Piguet, C., Paramagnetic Susceptibility by NMR: The "Solvent Correction" Removed for Large Paramagnetic Molecules. *J. Chem. Educ.* **1997**, *74*, 815.
81. Hogue, R. W.; Feltham, H. L. C.; Miller, R. G.; Brooker, S., Spin Crossover in Dinuclear N₄S₂ Iron(II) Thioether–Triazole Complexes: Access to [HS-HS], [HS-LS], and [LS-LS] States. *Inorg. Chem.* **2016**, *55*, 4152-4165.
82. Slichter, C. P.; Drickamer, H. G., Pressure-Induced Electronic Changes in Compounds of Iron. *J. Chem. Phys.* **1972**, *56*, 2142-2160.
83. Dei, A.; Poneti, G.; Sorace, L., Metal dilution effects on entropy and light-induced valence tautomeric interconversion in a 1:1 cobalt-dioxolene complex. *Inorg. Chem.* **2010**, *49*, 3271-3277.
84. Benelli, C.; Dei, A.; Gatteschi, D.; Pardi, L., Redox potentials and charge transfer spectra of catecholate and semiquinone adducts of a cobalt-tetraazamacrocyclic complex. *Inorg. Chim. Acta* **1989**, *163*, 99-104.
85. Shaikh, N.; Goswami, S.; Panja, A.; Wang, X.-Y.; Gao, S.; Butcher, R. J.; Banerjee, P., New Route to the Mixed Valence Semiquinone-Catecholate Based Mononuclear Fe^{III} and Catecholate Based Dinuclear Mn^{III} Complexes: First Experimental Evidence of Valence Tautomerism in an Iron Complex. *Inorg. Chem.* **2004**, *43*, 5908-5918.
86. Shimazaki, Y.; Tani, F.; Fukui, K.; Naruta, Y.; Yamauchi, O., One-Electron Oxidized Nickel(II)–(Disalicylidene)diamine Complex: Temperature-Dependent Tautomerism between Ni(III)–Phenolate and Ni(II)–Phenoxy Radical States. *J. Am. Chem. Soc.* **2003**, *125*, 10512-10513.

87. Rotthaus, O.; Thomas, F.; Jarjayes, O.; Philouze, C.; Saint-Aman, E.; Pierre, J.-L., Valence Tautomerism in Octahedral and Square-Planar Phenoxy–Nickel(II) Complexes: Are Imino Nitrogen Atoms Good Friends? *Chem. - Eur. J.* **2006**, *12*, 6953-6962.
88. Jeon, S.; Lee, H.; Lee, H. K.; Choi, Y.-K.; Jung, O.-S., Redox chemistry and valence tautomerism of cobalt-quinone complexes in nonaqueous solvents. *Bull. Korean Chem. Soc.* **1998**, *19*, 212-217.
89. Baydoun, H.; Mazumder, S.; Schlegel, H. B.; Verani, C. N., Deactivation of a Cobalt Catalyst for Water Reduction through Valence Tautomerism. *Chem. - Eur. J.* **2017**, *23*, 9266-9271.
90. Mondal, S.; Bera, S.; Maity, S.; Ghosh, P., Orthometalated *N*-(Benzophenoxazine)-*o*-aminophenol: Phenolato versus Phenoxy States. *ACS Omega* **2018**, *3*, 13323-13334.
91. Schrempp, D. F.; Kaifer, E.; Wadepohl, H.; Himmel, H.-J., Copper Complexes of New Redox-Active 4,5-Bisguanidino-Substituted Benzodioxole Ligands: Control of the Electronic Structure by Counter-Ligands, Solvent, and Temperature. *Chem. - Eur. J.* **2016**, *22*, 16187-16199.
92. Fumanal, M.; Jiménez-Grávalos, F.; Ribas-Arino, J.; Vela, S., Lattice-Solvent Effects in the Spin-Crossover of an Fe(II)-Based Material. The Key Role of Intermolecular Interactions between Solvent Molecules. *Inorganic Chemistry* **2017**, *56*, 4474-4483.
93. te Velde, G.; Bickelhaupt, F. M.; Baerends, E. J.; Fonseca Guerra, C.; van Gisbergen, S. J. A.; Snijders, J. G.; Ziegler, T., Chemistry with ADF. *J. Comput. Chem.* **2001**, *22*, 931-967.
94. Fonseca Guerra, C.; Snijders, J. G.; te Velde, G.; Baerends, E. J., Towards an order-N DFT method. *Theor. Chem. Acc.* **1998**, *99*, 391-403.

95. *ADF2014*, SCM, Theoretical Chemistry, Vrije Universiteit, Amsterdam, The Netherlands, <http://www.scm.com>.
96. Nagao, H.; Komeda, N.; Mukaida, M.; Suzuki, M.; Tanaka, K., Structural and Electrochemical Comparison of Copper(II) Complexes with Tripodal Ligands. *Inorg. Chem.* **1996**, *35*, 6809-6815.
97. Fuentes, O.; Paudler, W. W., Synthesis of 2-azacycl[3.2.2]azine. *J. Org. Chem.* **1975**, *40*, 1210-1213.
98. Piglosiewicz, I. M.; Beckhaus, R.; Wittstock, G.; Saak, W.; Haase, D., Selective Oxidation and Reduction of Trinuclear Titanium(II) Hexaazatrinaphthylene Complexes - Synthesis, Structure, and Electrochemical Investigations. *Inorg. Chem.* **2007**, *46*, 7610-7620.
99. Robinson, W. R., Perchlorate salts of metal ion complexes: Potential explosives. *J. Chem. Educ.* **1985**, *62*, 1001.
100. Cowieson, N. P.; Aragao, D.; Clift, M.; Ericsson, D. J.; Gee, C.; Harrop, S. J.; Mudie, N.; Panjikar, S.; Price, J. R.; Riboldi-Tunnicliffe, A.; Williamson, R.; Caradoc-Davies, T., MX1: a bending-magnet crystallography beamline serving both chemical and macromolecular crystallography communities at the Australian Synchrotron. *J. Synchrotron Radiat.* **2015**, *22*, 187-190.
101. *CrysAlisPro*, 1.171.37.35 or 1.171.38.43; Rigaku Oxford Diffraction: Yarnton, Oxfordshire, England, 2015.
102. Kabsch, W., XDS. *Acta Cryst.* **2010**, *D66*, 125-132.
103. Sheldrick, G. M. *SADABS*, University of Göttingen, Germany, 1996.

104. Sheldrick, G. M., Crystal structure refinement with SHELXL. *Acta Cryst.* **2015**, *C71*, 3-8.
105. Sheldrick, G. M., SHELXT– Integrated space-group and crystal-structure determination. *Acta Cryst.* **2015**, *A71*, 3-8.
106. Dolomanov, O. V.; Bourhis, L. J.; Gildea, R. J.; Howard, J. A. K.; Puschmann, H., OLEX2: A complete structure solution, refinement and analysis program. *J. Appl. Cryst.* **2009**, *42*, 339-341.
107. Bain, G. A.; Berry, J. F., Diamagnetic Corrections and Pascal's Constants. *J. Chem. Educ.* **2008**, *85*, 532.
108. Brahma, S.; Gardas, R. L., Understanding the solvation behavior of pyrrolidinium based ionic liquids in acetonitrile through thermophysical properties at 293.15 to 328.15K. *J. Mol. Liq.* **2018**, *256*, 22-28.
109. Morgan, S. O.; Lowry, H. H., Dielectric Polarization of Some Pure Organic Compounds in the Dissolved, Liquid, and Solid States. *J. Phys. Chem.* **1929**, *34*, 2385-2432.
110. Chorążewski, M.; Postnikov, E. B.; Oster, K.; Polishuk, I., Thermodynamic Properties of 1,2-Dichloroethane and 1,2-Dibromoethane under Elevated Pressures: Experimental Results and Predictions of a Novel DIPPR-Based Version of FT-EoS, PC-SAFT, and CP-PC-SAFT. *Ind. Eng. Chem. Res.* **2015**, *54*, 9645-9656.

SYNOPSIS. A DFT method using the OPBE functional was employed to screen a family of 25 complexes, resulting in the prediction of valence tautomerism for complex $[\text{Co}(\text{Me}_3\text{tpa})(\text{Br}_4\text{dioX})]^+$. This complex was synthesized and variable-temperature solution UV-visible absorption and magnetic susceptibility measurements confirm that it exists in a temperature-dependent valence tautomeric equilibrium between low spin Co(III)-catecholate and high spin Co(II)-semiquinonate forms.

